ESCUELA TÉCNICA SUPERIOR DE INGENIEROS INDUSTRIALES Y DE TELECOMUNICACIÓN

UNIVERSIDAD DE CANTABRIA

Trabajo Fin de Máster

DESARROLLO DE UNA APLICACIÓN PARA LA EVALUACIÓN DE PATRÓN DE RADIACIÓN DINÁMICO EN AGRUPACIONES DE ANTENAS

(Development of an application for the evaluation of dynamic radiation pattern in antenna array)

Para acceder al Titulo de

Máster Universitario en Ingeniería de Telecomunicación

Autor: Mariola Garayo Crespo

Junio -2024

MÁSTER UNIVERSITARIO EN INGENIERÍA DE TELECOMUNICACIÓN

CALIFICACIÓN DEL TRABAJO FIN DE MÁSTER

Realizado por: Mariola Garayo Crespo

Director del TFM: Ignacio Montesinos Ortego

Título: "Desarrollo de una aplicación para la evaluación de patrón de radiación dinámico en agrupaciones de antenas"

Title: " Development of an application for the evaluation of dynamic radiation pattern in antenna array"

Presentado a examen el día: 28 de Junio de 2024

para acceder al Título de

MÁSTER UNIVERSITARIO EN INGENIERÍA DE TELECOMUNICACIÓN

Composición del Tribunal:

Presidente (Apellidos, Nombre): De La Fuente Rodríguez, Luisa M.

Secretario (Apellidos, Nombre): Diez Fernández, Luis Francisco

Vocal (Apellidos, Nombre): Conde Portilla, Olga M.

Este Tribunal ha resuelto otorgar la calificación de: .....

Fdo: El Presidente

Fdo: El Secretario

Fdo: El Vocal

Fdo: El director del TFM
(sólo si es distinto del Secretario)

VºBº del Subdirector

Trabajo Fin de Máster Nº
(a asignar por la Secretaría)

Agradecimientos

Quiero tomarme un momento para agradecer a todas las personas que me han ayudado a lo largo de este viaje del trabajo fin de máster. Hay tanta gente que es imposible mencionar a todos, pero sepan que sin su apoyo, esto no habría sido posible.

Primero, gracias a mi familia, especialmente a mis padres, Francisco y Mariola, por su amor y apoyo constante. Gracias por creer siempre en mí y por darme el empuje necesario para seguir adelante.

A mi pareja, Jesús, no tengo palabras para expresar lo agradecida que estoy. Has estado a mi lado en cada paso del camino, día tras día. Tu paciencia, amor y comprensión han sido esenciales para mí, y no sé cómo habría llegado hasta aquí sin ti. A mis amigos, que son como una familia para mí, gracias por ser un pilar fundamental durante estos años, por el apoyo incondicional, por los momentos de risas y por estar ahí en los buenos y malos momentos.

A mi tutor, Nacho, quiero agradecerte de todo corazón por acogerme como discípula, y por compartir tu conocimiento y enseñanzas, tanto académicas como de la vida misma. Tu tiempo y dedicación realmente marcaron la diferencia. Se podría decir que cuando te conocí fui buscando plata, pero realmente acabé encontrando oro. No me puedo olvidar de mi experto en radiación, Pablo, siempre dispuesto a ayudarme y asesorarme, deslumbrándome con tu conocimiento. A Laura, por ser la editora más guapa y, sobre todo, tan joven que no ha dudado ni un segundo en ayudarme.

A la empresa Sener, por los recursos y oportunidades que me brindaron, permitiéndome desarrollar la beca de prácticas y completar este proyecto. También quiero agradecer el apoyo y la camaradería a todos mis compañeros de la oficina de Sener Santander.

Finalmente, quiero mostrar mi agradecimiento a los distintos profesores que han marcado mi camino estos seis años de grado y máster. Quiero destacar a aquellos que no solo hacen un trabajo encomiable, sino que me han iluminado con la luz que desprenden: José Ángel y Olga.

Este trabajo no solo representa un éxito académico, sino también un reflejo de todo el apoyo, cariño, amistad y guía que he recibido. Gracias de corazón a todos.

Abstract

The main objective of this Master's Thesis is the evaluation of radiation patterns of different antenna array configurations by means of an in-house developed graphical user interface. As inputs, the user will freely introduce a set of fundamental parameters such as relative distance, local distribution and for example the canonical radiating element to be employed as single unit.

To achieve this objective, one must understand the properties of the radiation patterns of the antennas and comprehend the effects of the interaction of different numbers of antennas. Based on theoretical foundations, it is necessary to delve into the mathematical modeling of phased arrays. Since various array configurations will be designed at the simulation level, they will be computationally modeled based on the results from the simulation environment.

The results obtained with the application perfetely match those obtained with full wave commercial solvers such CST Microwave Studio, validating the developed methodology and solver performance.

The conclusions focus on the similarity of the radiation patterns obtained in the simulation environment and the computational model prior to the interface design, and the easy access and usability of the application by the users.

List of Acronyms

ADC Analog-to-Digital Converter.

CPU Central Processing Unit.

DAC Digital-to-Analog Converter.

DBF Digital Beamforming.

DOA Direction of Arrival.

DPCA Displaced phase center antenna.

DSP Digital Signal Processor.

HRWS High Resolution Wide Swath.

ICW Interrupted Continuous Wave.

INSAR Interferometric Synthethic Aperture Radar.

LFM Linear Frequency Modulated.

RCS Radar Cross Section.

RF Radio Frequency.

SAR Synthetic Aperture Radar.

SLL Side Lobe Level.

SNR Signal to Noise Ratio.

TOPSAR Terrain Observation by Progresive Scans.

ULA Uniform Linear Array.

VAP Variable Phase and Amplitude.

Contents

List of Figures

Chapter 1

Introduction

1.1 Introduction

Karfid's proyect consist on develop the next generation Ka-band, Synthetic Aperture Radars (SAR) to earth observation missions, based on phased array antennas with hybrid analog-digital beamforming.

The activity aims to develop a receiver Rx front end with digital beamoforming for future radars, minimizing the power consumption, the overall cost of components and maximizing the integration in a restrained volume, which serves as a building block of larger and more complex systems. The building block will have complete functionality and scanning capabilities and will be susceptible to be used independently or in collaboration with other blocks of the overall larger array.

In the breadboard end to end performance of the system, it is important to identify the most critical drivers of the design:

- Power consumption: Special attention shall be put on power consumption optimization as far as this is one the main bottlenecks of phased arrays based on digital back-ends.
- Pointing accuracy: one of the key elements to have a good pointing accuracy and stability is the calibration algorithm. It is important to calibrate not only the RF chains but also the active impedance of the radiating matrix.
- Beam reconfigurability and multibeam: traditional analog phased array antennas could synthesize different radiation patterns modifying the complex excitation of each element. In this way new functionalities can be used such as nulling, beamwidth widening ... Multibeam will allow to simultaneously receive power of several areas.
- Fast beam scanning compared to mechanical scanning. Typically, a phased array can be reconfigured in microseconds. The reconfiguration time can be reduced if the beamformer has a small

memory that stores several configurations for several pointing directions. In this way the scanning speed can be greatly enhanced since the reconfiguration bottleneck is reduced. Moreover, with the hybrid beamforming approach, several digital beams can be synthesized around any analog beams, increasing vastly the scanning speed.

- Multiple Inputs Multiple Outputs algorithms. The antenna can be divided into several sectors and MIMO algorithms can be applied to improve the signal to noise and interference ratio. Although the project does not consider these algorithms, depending on the selected architecture, MIMO algorithms can be used in the future.

- Angle of arrival detection: the capacity of this feature will depend on the division between analog and digital beamforming.

In most critical aspects of the project, a study of the phased array's radiation pattern is required to achieve pointing precision in the desired direction. As the platform or target point moves, a reconfiguration of the main lobe for pointing at high speed is necessary. To design software and hardware capable of implementing these functionalities, engineers working on the project need simulation tools like CST or development environments like Matlab. These software tools, used for business or research purposes, require licenses plus any additional modules that drastically affect the available budget. Depending on the type of purchase, a software license maintenance program may also be required.

1.2 Objetives

The main objective of this project is to evaluate the radiation capabilities of any canonical microstrip antenna distribution in very short times. This will be achieved through the development of a user-friendly and intuitive graphical user interface in a programming language accessible to all users. To achieve the objective, the task is divided into several partial objectives.

- To study the radiation field of microstrip antennas at the simulation and computational level.

- To design microstrip antennas at the electromagnetic and computational simulation level in the frequency band of the Karfid project.

- To study the behavior of the generalized array factor and its fundamental properties.

- To study the different topologies of the array factor to be implemented.

- To compare and analyze the results of the radiation patterns of any cut from the different array factor configurations obtained computationally with the results of electromagnetic simulations.

- To develop a graphic user interface that easily allows the user to recreate any array distribution, evaluate its radiating performance and plot the results in easy-toread way.

1.3 Project Structure

This document is structured in 7 chapters subdivided into several sections:

- **Chapter 2: State of The Art.** The theoretical bases necessary to understand the principles of array factor and beamforming are studied to analyzed the operation of signal propagation with progressive phase shift to point to the desired direction.
- **Chapter 3: Synthetic Aperture Radar.** The operation of a SAR, its architecture and the different types of SAR technologies with various applications are described.
- **Chapter 4: Microstrip Antennas.** This part begins by contextualizing microstrip technology with respect to its main properties, feeding techniques and radiation patterns. Next, the design of micostrip patches is proposed at different initial frequencies from the literature to verify their simulation and computational results. Finally, design microstrip patches according to Karfid's project.
- **Chapter 5: Array Analysis of Different Configurations.** In this section, the results obtained in the simulation part and in the computational part are discussed. It focuses on certain array distribution structures and analyzes the differences that each type offers.
- **Chapter 6: Software Development.** This part explains the development of the software on each of the screens that make it up, the distribution of the elements on the screens and how they interact with each other.
- **Chapter 7: Conclusions and Future Lines.** This last chapter summarizes the results obtained and possible future lines to continue with the development of the software to the evaluation of different radiation patterns configurations.

Chapter 2

State of The Art

The main purpose of this chapter is to explain the theoretical concept of beamforming using an antenna array, steering the beam in a certain direction. All figures and documentation in this section have been taken from the engineering books [1, 2, 3, 4] and internet publications.

2.1 Introduction

In modern communications systems such as 5G Networks, Satellite communications and even for radar purposes, there is a tremendous need of agile beam steering, pattern composition and nulling. Such necesities rely on a set of independent but cooperative radiating element in a certain physical disposition. This, independent but cooperative radiating element in a certain physical disposition, called antenna array. The signals transmitted from different antennas are converted into waves that combine coherently in the air. This have a constructive or destructive effect.

The interest in having an antenna with high gain is to provide coverage to all users and adapt this coverage dinamically according to a required service. In such a grouping of antennas, the relative position and phase difference between, together with their individual amplitude determines the points of the space where the constructive and destructive interference happen. To actively change this steering direction, a beamformer is necessary to adjust the amplitude and delay of the signal transmitted from each antenna.

2.2 Array factor

The explanation of the array factor phenomenon involves two key perspectives. The first is from the perspective of signal processing, acknowledging that it identifies a channel through which to propagate and undergoes changes in the environment due to the constructive or destructive interference of other signals propagating through the channel. The second approach is from the microwave point of view,

conceptualizing the signal as a wave that emits an electromagnetic field and interacts with other electromagnetic fields. This section is going to explain array factor as using both methods.

2.2.1 Array factor as processing signal

The gain of an antenna is defined as a function of the ratio of intensity in a given direction to the radiation intensity that would be obtained if the power accepted by the antenna were radiated isotropically. The expression looks like:

$$G(\theta, \phi) = \frac{4\pi U(\theta, \phi)}{P_{in}} \tag{2.1}$$

Where $U(\theta, \phi)$ represents the radiation intensity in a given direction contained in the E_θ and E_ϕ fields compontens. P_{in} is the total input power accepted.

In a scenario where there are three antennas, two of them for transmission and the other one for reception. The transmission antennas will be assuming equality with the same expression for a sinusoidal signal transmitted, which could be expressed as:

$$x(t) = A \cdot cos(2\pi f_c \cdot t + \phi) \tag{2.2}$$

Where A represents the amplitude and ϕ the phase of the signal, and carrier frecuency f_c. Considering the distance between them like d and a distributed amplitude weighting.

$$w_1 = w_2 = 1/\sqrt{2} \tag{2.3}$$

Then, the array factor would be defined as:

$$AF(\theta, \phi) = w_1 + w_2 e^{jkdcos(\theta)} \tag{2.4}$$

The k is the relation between carrier frecuency and wave propagation speed c:

$$k = \frac{2\pi f_c}{c} \tag{2.5}$$

Using all of that and including a propagation delay τ and the path loss betwen antennas α, the expresion for the received sinusoid signal would be modeled as the product of all the components described before. It can be seen in the following equation:

$$y = \alpha e^{-j2\pi f_c \tau} AF(\theta, \phi) G(\theta, \phi) \tag{2.6}$$

Separating the array factor and the gain from the expression, that product represents the amplitude pattern for the array transmission, $g_A A(\theta, \phi)$.

2.2.2 Array factor as electromagnetic field

Based on the fact that a dipole-type antenna is formed by two conductors of equal length and opposite polarity, with a uniform current I_0 flowing through the conductors, generating an electromagnetic field, the radiation pattern produced is typically doughnut-shaped, with the strongest radiation perpendicular to the axis of the antenna and null points along the axis itself. This configuration results in the antenna having a directional pattern with maximum radiation intensity in the plane orthogonal to the conductors. The equations that model this behavior in the electric field and the magnetic field are described by Ampere's laws, Faraday's laws and Maxwell's equations. The expression for the electric field radiated by a dipole-type antenna can be reduced:

$$E_r = \eta_0 \frac{I_0 l}{4\pi} 2 \left(1 - j\frac{1}{kr}\right) cos\theta \frac{e^{-jkr}}{r^2} \tag{2.7}$$

$$E_\theta = j\eta_0 k \frac{I_0 l}{4\pi} \left(1 + \frac{1}{jkr} - \frac{1}{k^2 r^2}\right) sen\theta \frac{e^{-jkr}}{r} \tag{2.8}$$

In a complex scenario, where an antenna under study is an array of two horizontal dipoles situated over z-axis, each radiating a field, and taking into account the phase excitation difference between the elements (β), the total field is derived from the summation of the two individual fields.

$$E_t = E_1 + E_2 = j\frac{kI_0 l}{4\pi} \left(\frac{e^{-jkr_1 - (\beta/2)}}{r_1} cos\theta_1 + \frac{e^{-jkr_2 + (\beta/2)}}{r_1} cos\theta_2\right) \tag{2.9}$$

Assuming far-field $\theta_1 \approx \theta_2 \approx \theta, r_1 \approx r_2 \approx r \pm \frac{d}{2} cos\theta$, the equation could be rewritten as:

$$E_t = j\frac{kI_0 l e^{-jkr}}{4\pi} cos\theta \left\{2cos\left[\frac{1}{2}\left(kdcos\theta + \beta\right)\right]\right\} \tag{2.10}$$

Paying attention to the total far-zone field expression of the array, it is equal to the field of a single element at a selected reference point (normally the origin) multiplied by the array factor. The array factor of two elements is expressed as:

$$AF = 2cos\left[\frac{1}{2}\left(kdcos\theta + \beta\right)\right] \tag{2.11}$$

If it is generalizated for N elements it will be expressed as:

$$AF = \sum_{n=1}^{N} \frac{I}{\sqrt{N}} e^{j(n-1)\cdot(kdcos\theta + \beta)} \tag{2.12}$$

The array factor is a function of the number of elements, their geometrical arrangement, their relative magnitudes, phases, and spacings. In the formula mentioned earlier, the elements have identical amplitudes (I) and spacings, simplifying the equation.

The far-zone field of a uniform two elements array of identical elements, known as radiatrion pattern, is the product of the field of the single element at a selected reference point (usually the origin) and the array factor. That is:

$$PR = E_{single}(\theta, \phi) \cdot AF \tag{2.13}$$

Where PR represents radiation pattern, $E_{single}(\theta, \phi)$ reprents the electric field in θ and ϕ of a single element at reference point, and AF is the array factor.

The array configurations that will be studied in the following sections and will be developed throughout this project will be the linear array, planar array and circular array model.

2.3 Uniform Linear Arrays

A uniform linear array (ULA) is a common structure of antennas arranged in a row or a column. For the scope of the master's final project, the distance between elements is constant for canonic structures althought as it will be shown, randomize groupings could be also analyzed, usually less than a wavelenght. Moreover, all elements have the same amplitude pattern $g(\theta, \phi)$. The positions of N elements, denoted as d_n, are along the z axis for a vertical array and along the positive y-axis for horizontal array (see Fig 2.1).

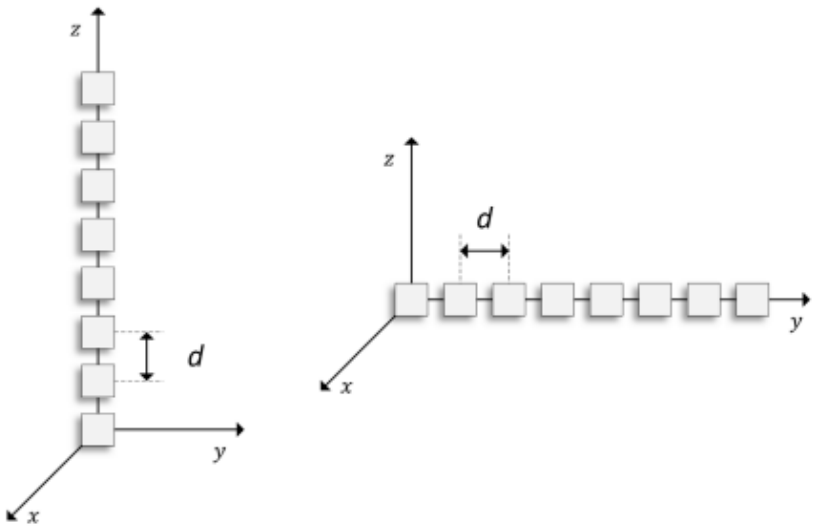

Figure 2.1: Example uniform linear array: vertical (left) and horizontal (right) [1].

The signals of all antennas are combined, resulting in an increased gain as a function of the direction (θ, ϕ). The maximum gain for an array with N elements is N times higher compared to a single antenna. Maximum gain occurs where all the elements' contributions are in phase, each of them with same amplitude. As a result, the gain increases for each element added in terms of N, it like $10log_{10}N$ dB.

$$G_T = G_{SE} + 10log_{10}N \tag{2.14}$$

When comparing a single antenna to an uniform linear array, the main lobe's beamwitdh decreases which means that the antena becomes more directive. Additionally, the number of nulls increases as the number elements increases. It is important to note that a null occurs when all the contributions sum destructively, causing the array factor becomes zero. This is defined in expression 2.11 for the contribution of 2 elements, but in the case of a linear array it will be observed as:

$$|AF(\theta,\phi)|^2 = N\left|cos\left(\frac{1}{2}\left(kdcos\theta+\beta\right)\right)\right|^2 \tag{2.15}$$

Then, when the expression 2.15 becomes zero, it implies that the first cosine term is $\pm\pi$, demonstrating that a null occurs at :

$$N\frac{kdcos\theta+\beta}{2} = \pm\pi \rightarrow \theta = cos^{-1}\left[\frac{1}{kd}\left(-\beta\pm\frac{2}{N}\pi\right)\right] \tag{2.16}$$

The number of N determine the order of the nulls, they will be a function of the element separation d and the phase excitation difference β.

It is necessary not only to increase the gain but also to adjust the direction with that maximum gain within a certain angle to cover all users. Beamforming allows dynamic adjustment in the direction without changing the mechanical orientation of the antennas. Specifically, this adjustment is achieved by changing the phase of the different elements so that the signal, combined by all the contributions from each component, arrives at the receptor at the same time.

2.3.1 Linear Array Along Other Cardinal Directions

It was explained before an uniform linear array distributed along, z-axis. It must be assumed that they are located along other cardinal axes [5].

An array factor distributed uniformly along x-axis its exponent will be written as:

$$x = kd\cdot sin\theta cos\phi, \qquad \beta = -kd\cdot sin\theta_0 cos\phi_0 \tag{2.17}$$

Considering that the radiation is normal to the x-y plane, $\theta = 90^{o}$, then $\beta = -kd\cdot cos\phi_0$. This result is similar an array along z-axis but with $cos\phi_0$ insted of a $cos\theta_0$. Thus, the pattern can be graphically constructed in the same way as for an array along the z-axis, but interpreting the physical angle as ϕ instead of θ. In another case, considering the radiation normal to the x-z plane, $\phi = 0^{o}$, then $\beta = -kd\cdot sin\theta_0$. This result is also similar to an array along z-axis but, it must be rotated 90 degrees, $sin\theta = cos(\theta-\pi/2)$.

An array factor distributed uniformly along y-axis its exponent will be written as:

$$y = kd\cdot sin\theta sin\phi, \qquad \beta = -kd\cdot sin\theta_0 sin\phi_0 \tag{2.18}$$

Considering that the radiation is normal to the x-y plane, $\theta = 90^{o}$, then $\beta = -kd \cdot sin\phi_0$. This result is similar an array along x-axis but with $sin\phi_0$ insted of a $cos\phi_0$.Thus, the pattern is relative to ϕ and needs to be rotated 90° after being constructed. In another case, considering the radiation normal to the y-z plane, $\phi = 90^{o}$, then $\beta = -kd \cdot sin\theta_0$. This result is also similar to an array along z-axis but, just like the other plane, it must be rotated 90 degrees.

2.4 Planar Array

A planar array can be viewed as a two-dimensional extension of an uniform linear array. In this section, only arrays with regular separation between elements with the same feeding are addressed. Suppose an array with m elements along the x and y axis n elements along the y axis. The total number of elements in this plane will be $m \cdot n$. The planar array function can be simply thought of as the combination of linear arrays in both directions. The total array factor for a planar array will be the product of the array factor of the elements on the x-axis and y-axis. Now the analysis of this can be thought of in a very simple way. What we do is take these linear matrices along the x axis, the elements are 1 to m. So it is a linear axis with even spacing of d_x, elements 1 to m can be combined with a single expression and that is given by its matrix factor:

$$AFx = \sum_{m=1}^{M} \frac{I}{\sqrt{M}} e^{j(m-1)\cdot(kd_x \cdot sin\theta cos\phi + \beta_x)} \tag{2.19}$$

The next step would be to consider the elements along the y axis with uniform spacing dy. Then the array factor for these elements can be expressed as:

$$AFy = \sum_{n=1}^{N} \frac{I}{\sqrt{N}} e^{j(n-1)\cdot(kd \cdot sin\theta sin\phi + \beta_y)} \tag{2.20}$$

Finally, the planar array factor expression will be the product of the linear arrays factor on both axis, such as:

$$AF = AFx \cdot AFy = \sum_{m=1}^{M} \frac{I}{\sqrt{M}} e^{j(m-1)\cdot(kd_x \cdot sin\theta cos\phi + \beta_x)} \cdot \sum_{n=1}^{N} \frac{I}{\sqrt{N}} e^{j(n-1)\cdot(kd \cdot sin\theta sin\phi + \beta_y)} \tag{2.21}$$

The main difference between a planar array and a linear array is that there are elements distributed along two axes. This allows beam adjustment in two planes, providing more precise and flexible control of beam direction. This is the fundamental principle of the phased array, which allows great flexibility in beam orientation without the need to physically move the antennas.

2.5 Circular Array

The circular array, where the elements are arranged in a circular ring, is a highly practical array configuration. Recently, circular arrays have been proposed for wireless communication, especially for

smart antennas. A circular array, the n elements are distributed uniformly along a circunference with a radious. Each element has defined an angular position (in this case x-y plane):

$$\phi_n = 2\pi \frac{n}{N} \tag{2.22}$$

So the circular factor array, is similar to a linear array along one axis but take into account the angular positiom, for this example will be expresed as (x-y plane):

$$AF = \sum_{n=1}^{N} \frac{I}{\sqrt{N}} e^{j(n-1)\cdot(ka\cdot sin\theta cosleft(\phi-\phi_n)+\beta)} \tag{2.23}$$

It represents a circular array of N elements equally spaced. The phase excitation of each elements will be:

$$\beta = -ka \cdot sin\theta_0 cos\left(\phi_0 - \phi_n\right)) \tag{2.24}$$

A significant advantage of a circular array over a linear array is its ability to provide 360-degree coverage in the horizontal plane without the need to physically rotate the antenna.

2.6 Classical Beamforming

Classical Beamforming is a technique to steer a beam in a certain direction by adjusting the phase of the transmitted signals, aiming to maximize the gain at the receiver in a specific direction. The main porpuse is to choose the shift of the signal, τ, so that the signals add constructively at a receiver in direction θ, ϕ. For n elements, this is represented as $\Delta\tau_n$. Moreover, the propagation delay difference depends on the path length difference, which it is related to the postion d_n, relative to a reference point as well as the direction of the receiver in terms of th wave vector k. These contributions and dependencies are satisfied by:

$$2\pi f_c \Delta\tau_{n(\theta,\phi)} = -d_n k(\theta,\phi) \tag{2.25}$$

The Fig 2.2 illustrates the behavior of the signal along the path and the delay between the array's reference point used to define the element positions and the receiving antenna. As the index n increases, the elements are farther away from the array, resulting in a longer propagation delay. Therefore, the transmission delay should be chosen as $\tau_1 > \tau_2 > ... > \tau_n$.

The signal $x(t)$, as per equation 2.2 with beamforming, is now modeled with the complex weight associated with element n and the implemented time delay.

$$x(t)_n = w_n x(t) \rightarrow w_n = \frac{1}{\sqrt{N}} e^{-j2\pi f_c \Delta\tau_{n(\theta,\phi)}} \tag{2.26}$$

From the previous expression, in the case of uniform linear array, significant results can be observed. For instance, with a vertical ULA consisting of N=8 elements, as shown Fig 2.1, separated by $d = 0.5\lambda$ and considering four different steering angles θ (90^o,110^o,130^o and 150^o), the gain pattern as a function

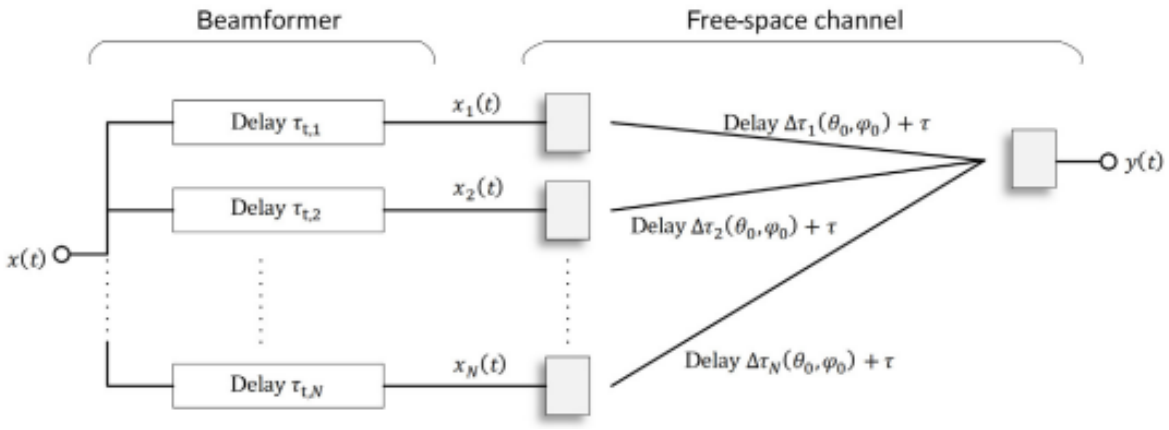

Figure 2.2: Scheme of the behavoir of same signals transmitted with different delay propagation [1].

of zenith angle θ for $\phi = 0^{\text{o}}$ is examined. The array is situated along z-axis where the direction of maximum radiation is perpendicular to the array ($\theta = 90^{\text{o}}$), is broadside radiation. An end-fire radiation have direction of maximum radiation along the axis of the array ($\theta = 0^{\text{o}}$ and $\theta = 180^{\text{o}}$).

As depicted in Fig 2.3, the main lobe's direction change by adjusting the transmission timing of the signal copies transmitted from different elements. Furthemore, it is observed that the direction at which the antenna gain of the array vector reaches its maximun does not fully coincide with the direction for which the array gain is maximed. Additionally, the maximum gain decreases with an increase in steering direction. Finally, the width of the main lobe increases as the angle between broadside and the steering direction increases. It is demostrated the direction of the main lobe in the maximum array gain depends on the beamforming weights, which can be specified in terms of zenith and azimuth angles θ and ϕ.

In the previous picture it was seen the influence of the steering angles on the directivity of the gain pattern, but it is also important to consider the distance between the elements. For example, in figure 2.4 are represented four differents distances between elements d ($3\lambda/4, /2, 1\lambda/4$ and $1\lambda/10$). It is observed that increasing the distance between the elements implies an increase in beam directivity, and the lobes become narrower. However, a greater distance not always be an advantage because appears a major number of secondary lobes which can generate interference. It is necessary to trade off and find a balance between high directivity and a low number of secondary lobes. In general, the compromise is a distance equal to $\lambda/2$.

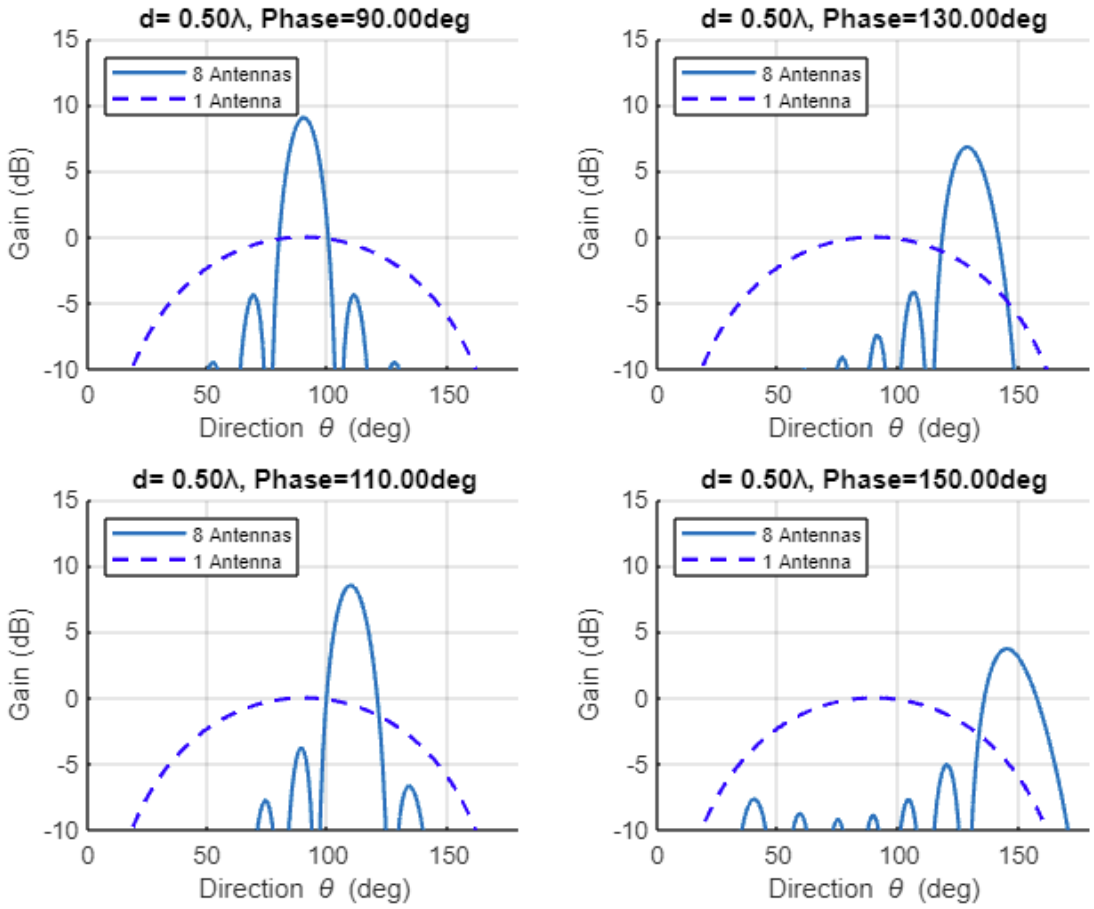

Figure 2.3: Gain pattern as function of θ for $\phi = 0^{\text{o}}$ and four different steering directions using a vertical array of eight elements separated by $d = 0.5\lambda$.

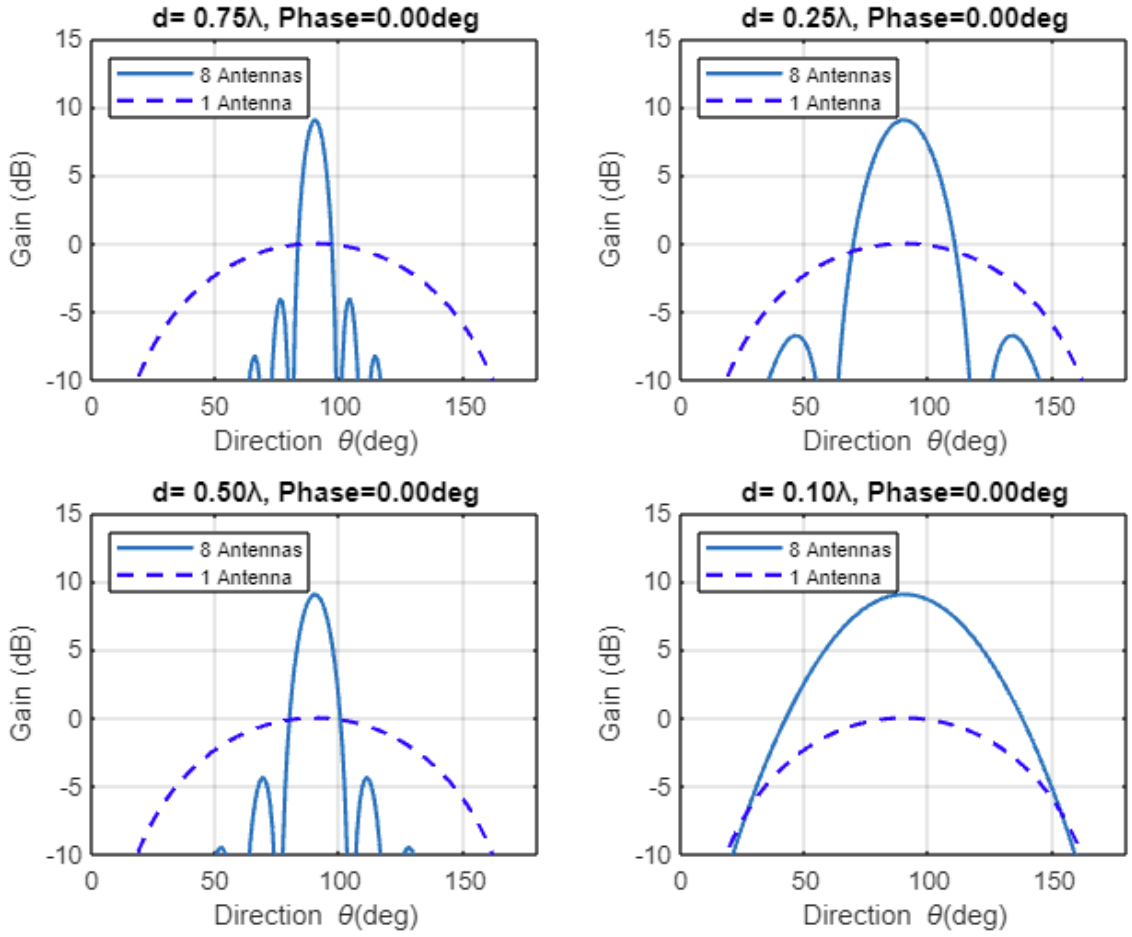

Figure 2.4: Gain pattern as function of θ for $\phi = 0^{o}$ and four different steering for directions using a vertical array of eight elements separated by differente distances d.

2.7 Array Architecture and Control Technology

The architecture of an array focuses on how elements can combine to provide amplitude weighting, phase or time delay, and adaptive control for interference suppression.

In the preceding sections, the importance and results of time delay steering have been explained. It consis on one Transmit/Receive (T/R) module and one time delay unit per element, providing small increments of time delay at each element. Then, the elements are grouped and amplified to compensate for the loss introduced by the time delay unit. Delays can be provided by analog or digital beamforming.

2.7.1 Analog Beamforming

The signals are generated in the digital domain and then converted into an analog signal through a Digital-to-Analog Converter (DAC), up-converted to a higher carrier frequency in the transmitter. In the case of the receiver, the process occurs in reverse with an Analog-to-Digital Converter (ADC). It is then connected to the network, where analog beamforming technology is composed of T/R switches to separate transmit and receive channels at the array level, followed by amplitude controllers that modify the signal level of the element to mitigate the impact of the sidelobes of the beams. This architecture includes simultaneous sum and difference beam formation.

Each beam is associated with phase shifters and attenuators to enable the beams to be dynamically directed in any desired direction. To effect a phase change, the phase shifters are connected to feedlines. Modern phased arrays with analog beamforming incorporate variable phase and amplitude (VAP) blocks at the radiating element level. All these is shown in Fig 2.5. After modifying amplitude and phase, the signals are combined to become one unique directional beam [6].

Despite the simplicity of the analog network implementation, the phase shifters and attenuators introduce losses and errors with degradations. Supporting multiple streams for various users and creating nulls in specific directions during transmission or reception becomes more challenging with an analog beamformer. The limitations of flexibility and lack of dynamic adaptation in analog beamformers can make it more difficult to adjust the configuration to meet the changing needs of multiple users or to establish precise nulls in specific directions. These challenges are more easily overcome through a digital beamformer, which allows for greater flexibility in configuration and more efficient adaptation to changing signal environment conditions.

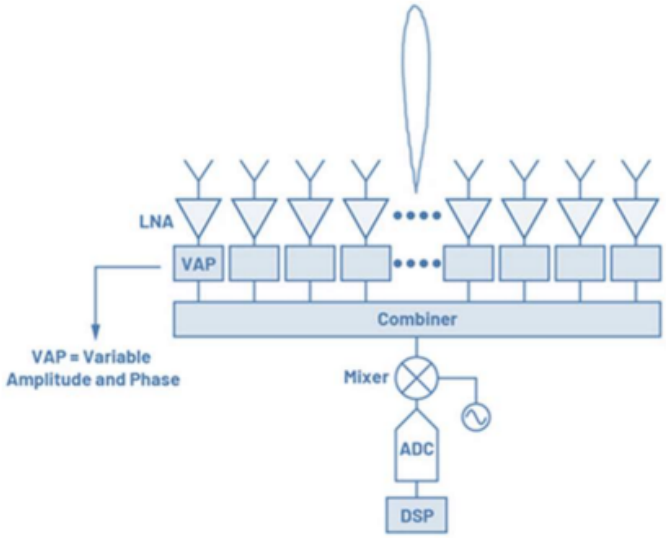

Figure 2.5: Analog beamforming schematic [6].

2.7.2 Digital Beamforming

This technique employs digital signal processing to dynamically and precisely adjust antenna beams. In this approach, signals are initially generated in the digital domain, providing greater flexibility and control over the process.

Each antenna in a digital beamforming system has its individual RF chain, including a set of analog-to-digital converters (ADC) and digital-to-analog converters (DAC). The digital beamformer independently adjusts the phases and weights of digital signals for each antenna element, achieving optimal precision through a digital signal processor (DSP) and field-programmable gate array (FPGA) matrices. It is shown in Figure 2.6 [6].

Digital signals are processed using DSP and FPGA, allowing for more precise and dynamic adjustments compared to analog techniques. The DSP is responsible for signal processing, such as adjusting phases and weights at the element level. In addition, you can count on specific calibration algorithms and models to ensure the accuracy and stability of the system. While the central processing unit (CPU) is responsible for monitors and controls beam adaptation, facilitating instantaneous changes in weights and phases to accommodate shifting environmental conditions and multiple user requirements. Additionally, it incorporates specific algorithms designed to optimize digital beamforming. Moreover, digital beamforming offers greater adaptability, allowing simultaneous formation of multiple beams with specific weights and phases.

One of the key advantages of digital beamforming is its superior adaptability and flexibility. The system can simultaneously form multiple beams, each with its specific weights and phases, catering to diverse communication needs. This adaptability extends to real-time adjustments, ensuring optimal

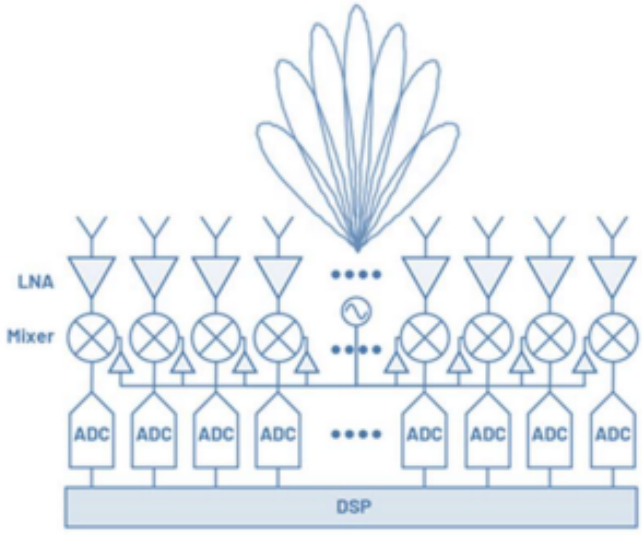

Figure 2.6: Digital beamforming schematic [6].

performance even in rapidly changing scenarios [7]. However, digital beamforming implementation suffers high power consumption and signaling overheads because there is one RF chain per antenna. For this reason, the hybrid model emerged, which is a compromise between the two models explained before.

2.7.3 Hybrid Beamforming

Hybrid beamforming is an innovative approach that aims to combine the strengths of both analog and digital models in beamforming. In this method, both analog and digital components are used together in the system, allowing for efficient optimization of performance. Instead of adopting one radio frequency (RF) chain per antenna, as in pure digital beamforming, the hybrid approach uses a reduced set of RF chains, each connected to multiple antennas. This significantly reduces power consumption compared to pure digital beamforming, as less hardware is required to handle multiple antennas. A basic schematic is shown in Fig 2.7.

The implementation of hybrid beamforming involves dividing tasks between analog and digital components. The analog part of the system handles the initial adjustment of beams and beamforming at a broader level using analog components like switch networks and phase adjustments. On the other hand, the digital part of the system fine-tunes and dynamically adjusts beams through digital signal processing (DSP), allowing adaptation to changing conditions and dynamic performance optimization [6].

To ensure system coherence and accuracy, calibration is performed at both analog and digital levels. Analog calibration adjusts analog components to ensure precise alignment between antennas and RF

chains. Digital calibration optimizes fine adjustments made at the digital level, ensuring overall system coherence and accuracy.

In summary, hybrid beamforming aims to achieve improved efficiency and adaptability by combining the effectiveness and low complexity of the analog part with the flexibility and adaptability of the digital part, resulting in a more balanced and efficient beamforming system.

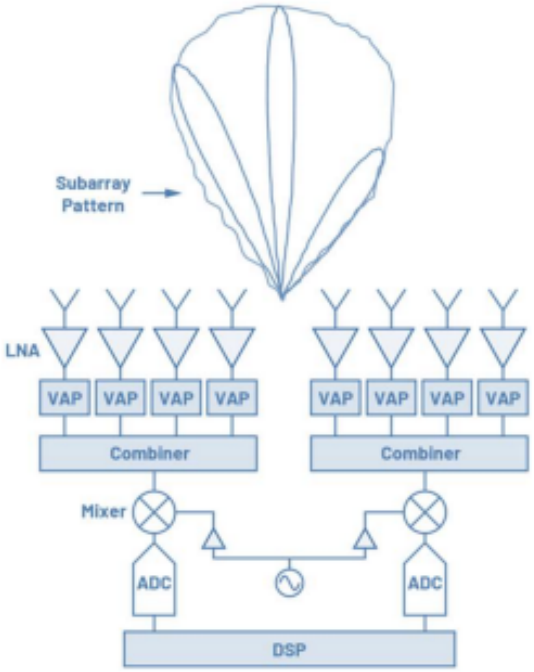

Figure 2.7: Hybrid beamforming schematic [6].

2.8 Trade-off conclusion

Comparision of beamforming architecture and processing. Front end trade off conclusions it seen in table 2.1.

Beamforming	Multibeam Capabilities	Architecture complexity	Radiation Patter Definition	Beam agility
Analog	Limited to two or four beams if COTS beamformers allows it	High if COTS beamformers are not used. Otherwise is low	Perfectly shaped patterns after calibration	Low it the CoreChips do not include memories for position recording
Digital	Limited to the processing capability of the Back-end	High	Perfectly shaped patterns after calibration	Maximum
Hybrid	Limited to the COTs CoreChips and the digital beams will be steered around the possible analog ones	Mid	Patterns with shape, null depth and gain depending on the size of sub-arrays	The sub-array with analog beamforming will be low in the plane that contains the columns if the CoreChips do not include memories
	Digital Post Processing	Power Consumption	Cost	Mass
Analog	Not available	Low	Low	Med
Digital	Fully processable	High		High
Hybrid	Processable at sub-array level	Mid	Mid	Mixed

Table 2.1: Front-end trade-off

Chapter 3

Synthetic Aperture Radar (SAR)

3.1 Introduction

Synthetic Aperture Radar (SAR) systems are advanced imaging tools that emit microwave electromagnetic radiation across frequencies ranging from 300 MHz to 300 GHz. Unlike optical imaging systems, which rely on solar electromagnetic radiation within the visible spectrum, SAR systems actively illuminate the scene they're observing with their own transmitted signal [8].

SAR finds applications in various fields such as intelligence gathering, surveillance, reconnaissance, interferometry, foliage penetration, moving target detection, and environmental monitoring. One of SAR's key advantages over optical imagers is its ability to operate independently of daylight and visibility conditions, making it particularly useful in diverse environments. At a fundamental level, SAR systems emit microwaves towards a scene and measure the voltage returned from different targets within that scene. This voltage data is then used to determine the radar cross-section (RCS) of each target, indicating how prominently it appears in the radar image. Targets with high RCS values appear bright, while those with low RCS values appear dim. Manmade structures like buildings, vehicles, and roads typically exhibit high RCS values due to their rough surfaces, which scatter electromagnetic radiation back towards the radar. In contrast, the relatively flat ground tends to scatter EM radiation away from the radar, resulting in lower RCS values.

3.2 SAR functionality

It has been previously explained that SAR uses a short-pulse, single-frequency radar signal against the Earth's surface to measure the reflected signal and reconstruct a high-resolution image.In specific, the antenna gets the phase and amplitude of the radar reflected signal. Interrupted Continuous Wave (ICW) SARs have a duty cycle of less than 100%. The brief pulse duration requires high instantaneous power to maintain a good signal-to-noise ratio (SNR). Most SAR systems today use a Linear Frequency

Modulated (LFM) signal. An LFM signal, often known as a "chirped" signal, changes frequency linearly during the pulse duration. The amplitude of the transmitted waveform is constant during the pulse time τ, while the instantaneous frequency varies linearly with time τ according to $f_i = k_r\tau$, where k_r is known as the chirp rate, producing the bandwidth $B_r = k_r\tau$. In other words, the range of frequencies in an LFM signal determines its bandwidth [9].

LFM signals also have longer pulse lengths than those of ICW systems, so they carry more energy per pulse than ICW signals, thus decreasing the instantaneous power requirement. A narrow pulse width poses a challenge in achieving a reasonable Signal-to-Noise Ratio (SNR), which is typically a crucial performance metric for radar systems. Linear Frequency Modulation (LFM) Synthetic Aperture Radar (SAR) systems circumvent this issue by allowing the lengthening of pulse duration to boost total transmit energy without compromising range resolution.

The mathematical expression for a zero phase LFM transmit signal can be :

$$s_t(t) = A(t) \cdot exp(j(2f_0t + k_rt^2)) \tag{3.1}$$

where $A(t)$ is the signal amplitude as a function of time t, f_0 is the initial frequency of the chirp, and k_r is the chirp evolution rate. The transmitted signal propagates through the atmosphere with an inherent propagation loss and is scattered throughout the target scene. In most of the cases, the majority of the energy transmitted scatters away from the radar receiver, in such a way that the total received energy is very low.

$$s_r(t) = A'(t) \cdot exp(j(2f_0(t-\tau) + k_r\left[(t-\tau)\right]^2)) \tag{3.2}$$

where $A'(t)$ is an attenuated version of $A(t)$ and τ is the two-way time of flight from the radar to the target at range R, and is given by :

$$\tau = \frac{2R}{c_0} \tag{3.3}$$

3.3 SAR acquisition modes

SAR has developed different technologies to make a varied type of scanning modes in order to carry out with the requirements of each mission. In this section will be presented the main principales. This modes are described in, [10, 11, 12, 13].

3.3.1 Stripmap

StripMap mode operates by continuously illuminating a narrow strip of the Earth's surface with radar pulses while the satellite moves along its orbit. The antenna boresight is in a fixed Position emits radar pulses perpendicular to the satellite's direction of motion, ensuring a constant swath width, as it

can see in Figure 3.1. This mode offers moderate swath coverage and high spatial resolution, making it suitable for detailed mapping and terrain analysis applications. StripMap SAR images exhibit high spatial fidelity and clarity, making them ideal for tasks such as land cover classification, urban planning, and environmental monitoring. The consistent resolution along the strip enables accurate measurement of surface features and changes over time, making StripMap mode a valuable tool for scientific research and resource management.

3.3.2 Scan

ScanSAR mode utilizes a unique beam-scanning technique to achieve wide swath coverage over large geographic areas. The radar antenna system divides the radar beam into multiple smaller sub-beams, each covering a distinct swath on the ground, Figure 3.1 ilustrates this mode. These sub-beams are emitted at different angles, allowing for coverage of a wide area despite the satellite's motion along its orbital path. ScanSAR sacrifices spatial resolution in favor of coverage, making it suitable for monitoring broad-scale environmental phenomena and natural disasters. This mode is particularly well-suited for applications such as deforestation monitoring, sea ice mapping and disaster response.

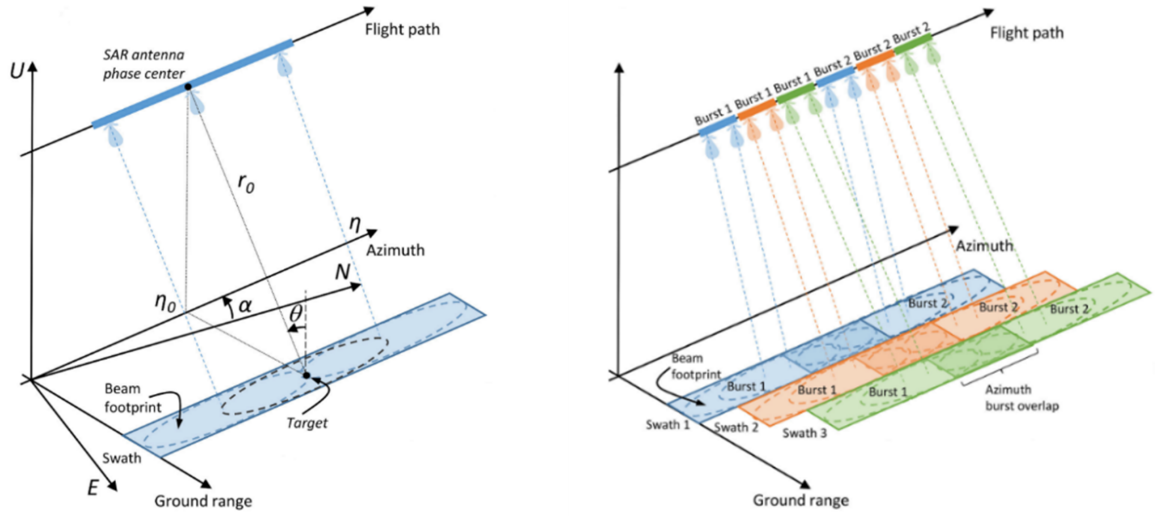

Figure 3.1: Left figure Strip SAR mode and right figure Scan SAR mode [11].

3.3.3 Terrain Observation by Progressive Scans (TOPSAR)

Terrain Observation by Progressive Scan (TOPS SAR) mode combines the advantages of stripmap and ScanSAR modes by employing a continuous beam-steering technique while maintaining high spatial resolution. The satellite dynamically adjusts the radar beam direction during data acquisition using electronically scanned array antennas, as it can see in Figure 3.2 . This allows for progressive scanning of the terrain, ensuring uniform resolution across the swath and mitigating the effects of terrain-induced distortions. TOPS SAR utilizes advanced signal processing techniques. This mode is well-suited for applications requiring accurate terrain information, such as land cover classification, geological mapping, and infrastructure monitoring, where both coverage and resolution are essential.

3.3.4 Spotlight

SpotSAR is a specialized SAR mode engineered to provide exceptionally high-resolution imaging of specific targets or areas of interest. In SpotSAR mode, the radar antenna system dynamically forms and directs a narrow radar beam towards a designated spot on the Earth's surface. This precise targeting allows for the acquisition of detailed radar imagery with superior spatial resolution. As the satellite maneuvers along its orbit, the antenna system adjusts its orientation to maintain focus on the designated spot, optimizing illumination and imaging conditions, as Figure 3.2 ilustrates. SpotSAR employs advanced signal processing techniques to enhance image quality and detail, making it well-suited for applications requiring precise mapping of urban areas, infrastructure monitoring, and reconnaissance missions. The ability to precisely target and image specific spots on the Earth's surface enables SpotSAR to provide valuable insights into surface features and changes.

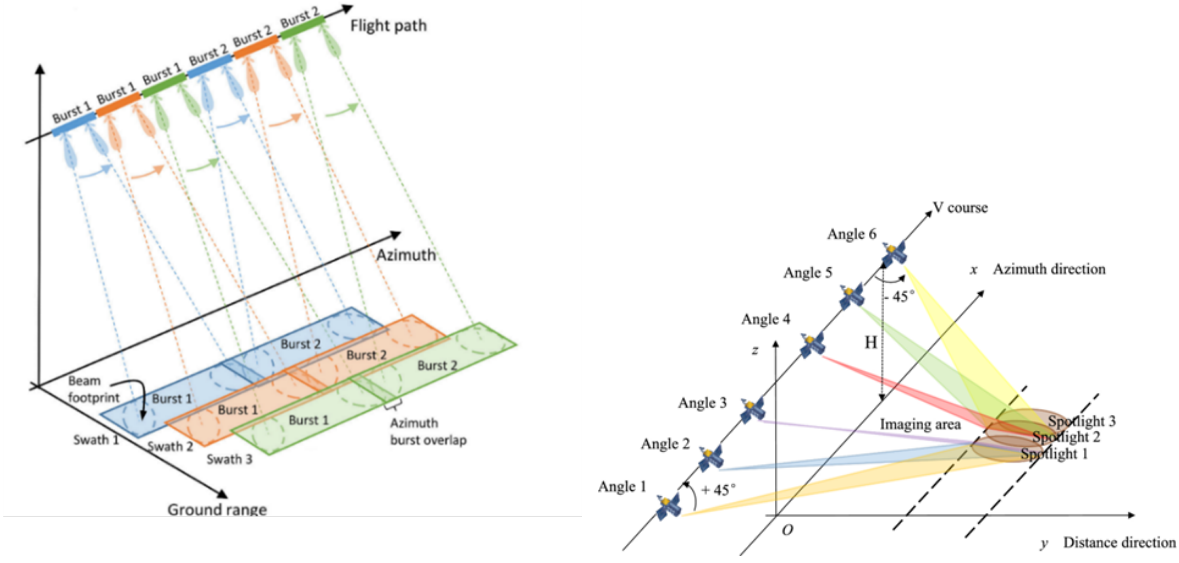

Figure 3.2: Left figure TOPSAR mode and right figure Spot SAR mode [11] [12].

3.3.5 High Resolution Wide Swath (HRWS)

The two most critical features of modern SAR systems—azimuth resolution and swath coverage—are inherently contradictory in their design. To address this, HRWS SAR has been introduced. This system uses a small, separate antenna for transmitting radar signals, and multiple sub-antennas in both elevation and azimuth for receiving echoes. Unlike traditional monostatic SAR, HRWS SAR employs adaptive beamforming and displaced phase center antenna (DPCA) technologies for elevation and azimuth, respectively.

The HRWS SAR system utilizes multiple elevation antennas and digital beamforming (DBF) to create a precise, high-gain pattern that tracks the direction of echoes in real-time. The weighting coefficients for each channel are adjusted over time, a method known as SCORE (scan-on-receive). The direction of arrival (DOA) is calculated based on the vertical slant-range plane geometry, assuming a perfectly spherical Earth model, ignoring topographic variations. However, in real-world scenarios with varying terrain, the actual DOA deviates from the preset DOA, leading to pattern loss compared to ideal conditions.

The HRWS SAR system's DPCA technique uses multiple apertures in azimuth to collect additional samples for each transmitted pulse along the synthetic aperture. This increases the pulse repetition frequency (PRF), allowing for the unambiguous mapping of a wider swath. However, to ensure uniform distribution of these azimuth samples, the PRF selection is constrained: the SAR platform must move exactly half its antenna length between successive radar pulses. This strict PRF condition often conflicts with the optimal design of other system parameters. If not met, periodic nonuniform sampling in azimuth occurs, resulting in azimuth ambiguities when using traditional imaging algorithms based on matched filtering.

This mode is particularly well-suited for applications requiring comprehensive monitoring of vast regions, such as surveillance, reconnaissance, disaster response, and environmental monitoring. HRWS enables detailed mapping of complex terrain features, detection of small-scale changes, and enhanced situational awareness over extensive areas, making it a valuable tool for scientific research, resource management, and security applications.

3.3.6 Interferometric SAR (INSAR)

Interferometric SAR, or InSAR, is a specialized SAR technique that leverages the phase difference between two or more radar images of the same area to extract topographic and deformation information. InSAR operates by comparing the phase of radar signals received from the Earth's surface at different times or from different viewing angles. By measuring the changes in phase, InSAR can detect subtle surface deformations, such as subsidence, uplift, or changes in the Earth's crust, Figure 3.3 ilustrates this mode. InSAR requires precise satellite positioning and high coherence between radar

images to accurately measure surface changes. This technique is widely used in geodesy, geophysics, and environmental monitoring for applications such as mapping ground motion, monitoring volcanic activity, and assessing land subsidence. InSAR provides valuable insights into surface processes and can help mitigate risks associated with natural hazards and human-induced activities.

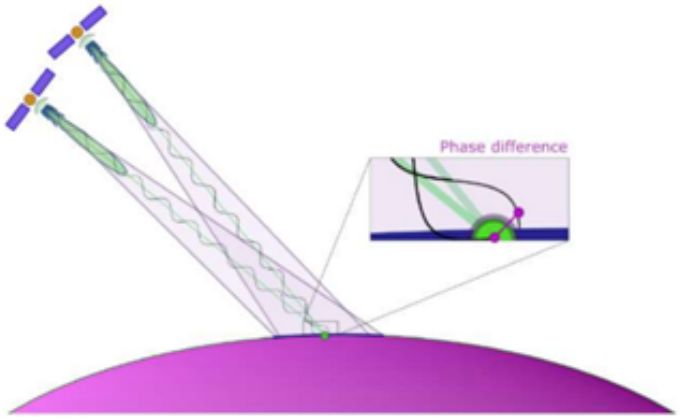

Figure 3.3: Interferometric SAR mode [10].

3.4 SAR instrument architecture

The SAR instrument architecture as shown in Figure 3.4, together with the main that the services that the platform shall provide: the power supply unit and the SAR generated data storage. SAR instruments is divided into three main parts:

- Active Electronically Scanned Array (AESA) is composed by several tiles with analog beamforming, which receives the scattered signal from the target and delivers it to the RF subsystem in two independent and orthogonal components in V and H. The frequency of operation and the pointing needs will define the minimum distance between single radiating elements and, therefore the lvel on integration needed for the rest of the RF circuitry. It is intended to include a LNA right after each polarization terminal at the single element level.

- RF and electronics. The filtering, singal level conditioning, singal down conversion is carried out in this section of the instrument. Each tile will deliver two channels per element row, one per polarization, reaching the ADC terminalsof the multiple RFSoC systema that composes the digital back end.

- The digital backend which is responsible for analog beamforming control of the AESA tiles, the RF subsystem control and to provide the digital beamforming according to the acquisition mode.

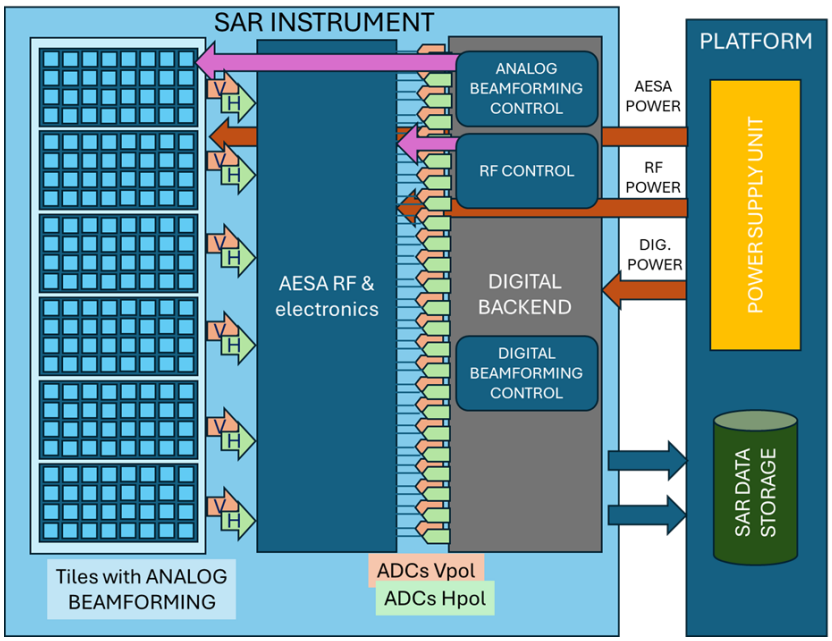

Figure 3.4: SAR instrument architecture.

3.5 Karfid's Preeliminary Architecture

Karfid proyect is designed to spaceborn of Syntehtehic Aperture Radars to earth observation missions in Ka-band. It is based on phase array antennas with hybrid analog-digital beamforming.

The design and development of a building block architecture to serve as a unit brick to compose bigger antenna arrays and systems, able to adapt to several platforms and missions. This building block consists of three main parts: phased array antenna tile, RF chain and digital back end. Figure 3.5 ilustrates the diagram block. Firstly, the phased array provides beam scanning capabilities, composing analog beamforming in one axis and digital beamforming in the other. Each column is composed of eight dual-polarized radiating elements, which add up to 32 patches distributed along four columns. Every column is connected to its corresponding beamformers (BFICs), that are preceded by an LNA per radiating element to ensure a los system noise figure.

After the LNA and the beamformers, the down conversion stage is in charge of lowering down in frequency the received signals, prior to be delivered to the digital back end. Initially, this conversion will be done in a single step with a I/Q subharmonic down converter, reducing the number of required components, the required size and the total losses in the RF chain. Signals are transformed to an adequate IF frequency band which permits a graceful digitalization according to the ADC capabilities. This IF section also includes a signal level control to adapt the incoming signal dynamic range to the power range of each ADC.

The digital back end section converts the RF signal with the ADCs, demodulates, processes and stores the gathered data. The computation capacity and the ADCs rate is critical for an overall optimal system operation.

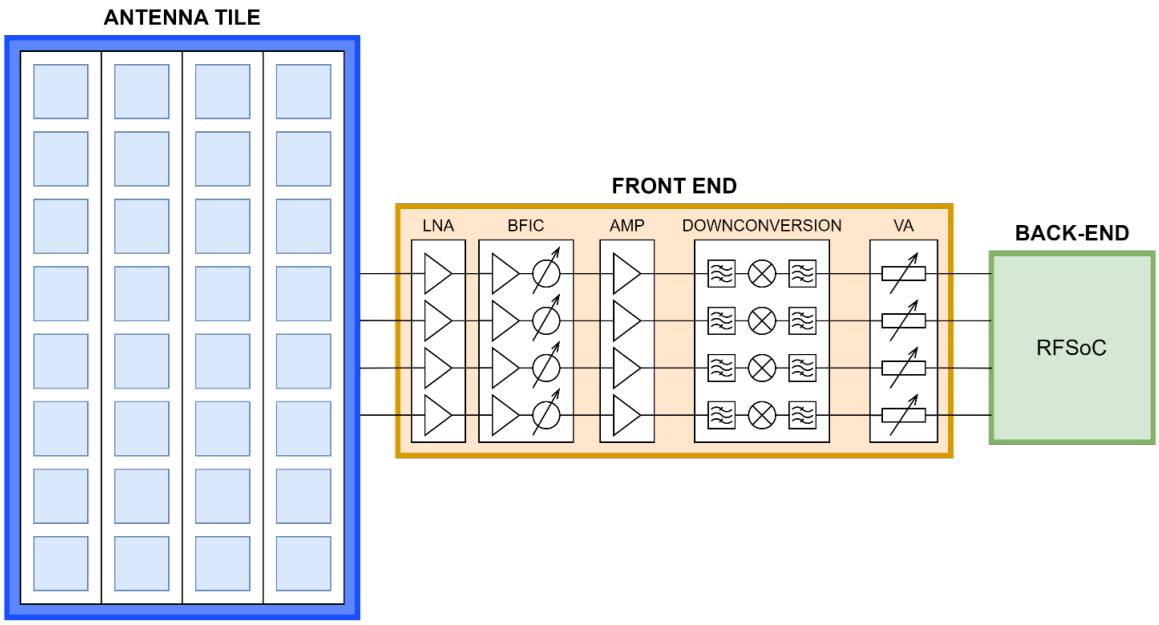

Figure 3.5: System architecture block diagram.

Chapter 4

Microstrip Antennas

The main purpose of this chapter is to introduce theoretical concepts of microstrip antennas, which will be used in this project. The objective is to compare experimental results with therorical results established in the scientific community. Most figures and documentation in this section have been taken from the engineering books [3] and internet publications [14].

4.1 Introducction

As explained in the previous chapter, the objective of Karfid project's application is to develop a breadorad receiving system able to be used as single unit of a bigger aperture to work in Synthetic-Aperture Radar specifically with a Scan-On-Receive mode. To achieve this goal, it is required to implement antennas with certain characteristics: low weight, small size, cost-effectiveness, easy integration, and aerodynamics. Microstrip antennas already meet this profile; they are versatile in terms of resonant frequency, polarization, pattern, and impedance. Additionally, these characteristics can be designed simply by adding loads between the patch and the ground plane.

The key to their utility lies in the fact that they can be fabricated using low-cost lithographic techniques on printed circuit boards. Moreover, they can be produced using monolithic integrated circuit techniques, all through automated processes.

4.2 Main Properties

Microstrip antenna consists of three elements; radiation patch, dielectric substrate and ground plane, as shown in figure 4.7. The radiation patch is a thin metallic strip $t << \lambda_o$ (λ_o refers to free space wavelength), with a length L tipically $\lambda_o/3 < L < \lambda_o/2$ and width W. The strip line is placed above the dielectric substrate, which width is usually between $0.003\lambda_o \leq h \leq 0.005\lambda_o$, depending on the substrate selected. In general, the dielectric constant of the substrates that can be used for the design of microstrip antennas, usually in the range of $2.2 \leq \epsilon_r \leq 12$. The best option for a great functionality

of antenna is thick substrate with a dielectric constant in the lower end of the range because this offer close limits in fields for the dispersion of radiation into space. Finally, the other side of the substrate is in contact with the ground plane, and acts as a reflection for radio waves. It ensures that radio waves are directed in the correct direction.

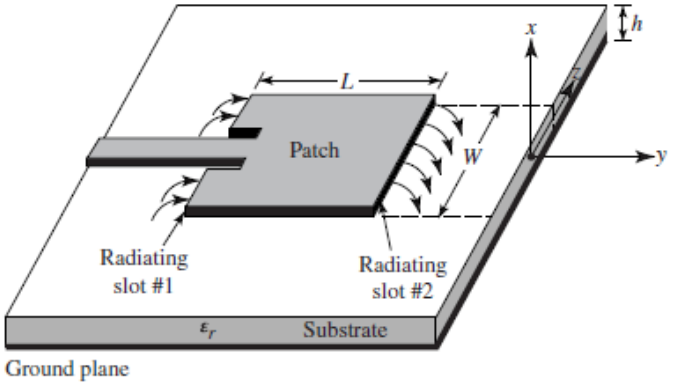

Figure 4.1: Microstrip antenna system [3].

Depending on the specific requirements to design microstrip antenna, there exists multiple types of feeding configuration. The radiation patch may be a dipole, rectangular, square, circular, ellipitical, triangular, or any other configuration. The common ones are square, circular, rectangular and dipole, in this chapter is going to be emphasis in circular and rectangular types. They are commonly used because of ease of analysis and fabrication, and their radiation characteristics.

The radiation pattern of the strip antenna is omnidirectional, even though power radiation predominantly emits towards the upper part of the antenna in its ideal configuration, as it considers an infinite ground plane. This blocks radiation to the lower part of the antenna. This is the reason why the maximum radiation pattern is normal to the patch (broadside radiator).

In reality, it could exists radiation to lower part of the antenna as the dimensions of ground plane continue to be finites. However, the secondary lobes are smaller ones in comparisation to principal lobe so they are despicable.

4.2.1 Feeding Methods

There are many configurations that can be used to feed microstrip antennas in order to get radiated efficiency in desirable frecuencies with a correct impedance coupling. The four most popular are the microstrip line, coaxial probe, aperture coupling and proximity coupling.

Microstrip line feed

The microstrip-line feed consists in feed the radiaton patch that is connected direct with the microstrip line. This method is easy to fabricate, simple to match by controlling the inset position and rather simple to model. However, it presents the worst efficiency in regards to band width and coupling, owning to substrate thickness increase so surface waves and spurious feed radiation increase.

To feed an antenna with a microstrip line could be by directly connecting the radiation patch with the antenna edge, in this case the coupling impedance will be better depending on the line microstrip position with respect to the patch. Another option, could be by inserts, the deep of the inserts establish the coupling of the impedance.

Coaxial-line feed

This method involves attaching the inner conductor of the coaxial cable to the radiation patch, while the outer conductor is connected to the ground plane. This technique is commonly used for feeding microstrip antennas. However, it presents difficulties because the conductive pin of the coaxial cable must pierce through the substrate, which is very thick.

Proximity coupled feed

In this method, electromagnetic coupling is used instead of direct contact. The radiation patch is located above a dielectric substrate, and in the lower part of the structure, there is a feed line on top of a feed dielectric substrate. The second dielectric substrate layer is above the ground plane. The first layers are usually wider and have a low dielectric constant. The second layers, the feed ones, are thicker and have a high dielectric constant.

Aperture-coupled feed

The aperture coupling is similar to proximity coupling because it also employs two dielectric substrate. In this case, the substrates are separated by a ground plane. On the bottom side of the lower substrate there is a microstrip feed line whose energy is coupled to the patch through a slot on the ground separating the two substrates. The advantage here is the line feed located in the lower part and separated from the atenna by the ground plane, so the radiation of the line feed is minimum in the direction of the radation from de antenna so there are not interferences or cros-polarization.

4.2.2 Methods of Analysis

The method of analysis of an antenna is determinate their main properties such as the radiation pattern, gain, losses, effieciency. There are many methods of analysis for microstrip antennas. The most popular models are the transmision-line, cavity and full wave.The full-wave model is the most

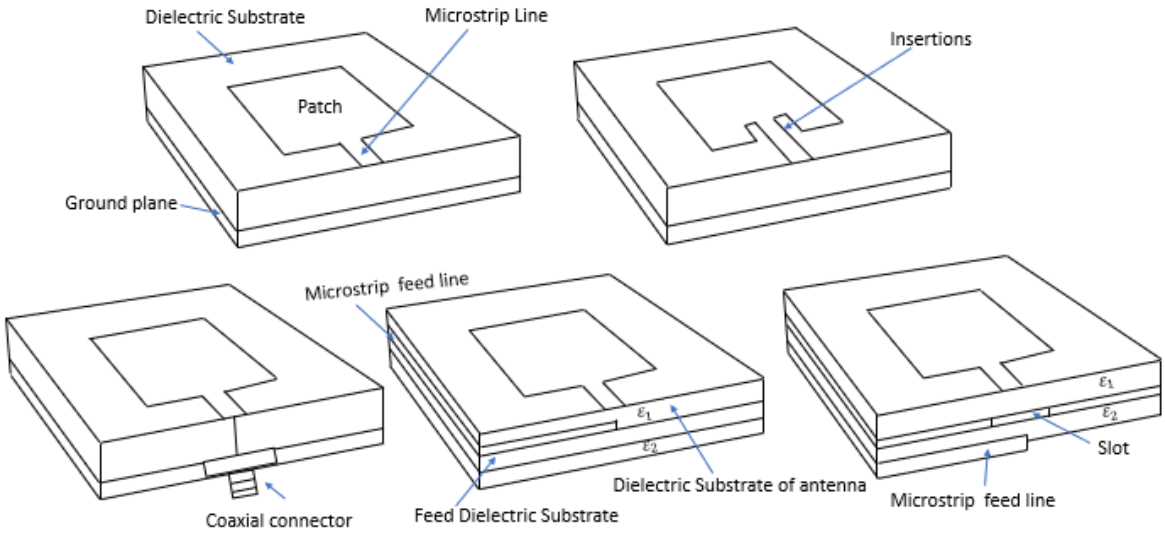

Figure 4.2: Typical feeds for micstrip (Above: from right to left direct microstrip line feed and insertions microstrip line feed, Below: from right to left coaxial line feed, proximity coupled feed, aperture coupled feed).

complex. Therefore, it will explain the transmission model and the cavity model, which, due to their simplicity, make it easier to study field behavior.

Transmision Line Model

The transmission line model is used for the design of circular and rectangular antennas. This model represents the patch antenna as two radiating narrow slots separated by a low impedance transmission line. The slots could be considered as two complex admittances formed by a conductance G and a susceptance B.

The field distribution along the edges of the antenna presents fringing effects. The amount of fringing is a function of the dimensions of the patch and the height of the substrate. These effects appear in the air and the dielectric substrate of the antenna, so for that, the antenna uses two different dielectric constants. Moreover, the effective length of the antenna is different from the physical length due to fringing effects. In this model, it is supposed that the effective dielectric constant is a combination of the air dielectric constant and substrate dielectric constant, and it is assumed that the antenna is inside a homogeneous environment.

The first step in the design is to specify the frequency of operation and select the substrate, then calculate the effective width of the antenna from the dielectric constant substrate, frequency of operation, and substrate height. Then, the following steps involve calculating the length variation taking

into account the fringing effects to estimate the real length for designing the antenna.

Cavity Model

This model considers the microstrip as a cavity plane that presents higher-order resonances, allowing radiation through its edges. To analyze the normalized fields within the dielectric substrate between the patch and the ground plane, this region is considered a cavity limited by electric conductors and magnetic walls along the perimeter of the patch. The magnetic side walls are slots where radiation takes place.

When the microstrip patch is energized, a charge distribution is established on the upper and lower surfaces of the patch. The charge distribution is controlled by attractive and repulsive mechanisms. The attractive mechanism occurs due to opposite charges on the bottom side of the patch and the ground plane, while the repulsive mechanism occurs due to the same charges on the bottom surface of the patch. This mechanism tends to move a part of the charge from the bottom of the patch toward the edges to the upper surface. The movement of the charges creates current densities Jb and Jt on the bottom and top surfaces of the patch.

In practice, the ratio between height and width is very small, and the dominant mechanism is attractive, with the charge and current flows remaining around the edges of the patch and attaching to the upper surface. Thus, the magnetic tangential patch at the edges is not zero, and in the cavity model, side walls are modeled as perfect magnetic conductors. This model produces good normalized electric and magnetic field distributions beneath the patch.

The field configuration within the cavity can be found using the vector potential approach, which must satisfy the homogeneous wave equation. The solution of these equations proposes even numbers kx, ky and kz alog the x, y and z axes. These will be determined subject to the boundary conditions. Finally, the wavenumbers can be calculated to determine the number of half-cycle field variations along the axes, and with that, along with physical dimensions, resonant frequencies for the cavity can be determined to complete the design.

4.3 Radiation Pattern

This section aims to analyze the radiation field of canonical microstrip patches as suggested by A. K. Bhattacharjee et all [15], to compare theoretical models with a method for calculating the far field from the equations also proposed by A. K. Bhattacharjee et all [15]. For this analysis, it will be assumed that the patches are located in the x-y plane and radiate towards the z-axis.

4.3.1 Rectangular Patch

In the case of rectangular patch, the mathematical description of the Electric field can be written in terms of the cartesian or the spherical coordinates. According to the first ones:

$$|E_x| = |w \cdot sinc(k \cdot a \cdot u/2) \cdot cos(k \cdot a \cdot u/2)| \tag{4.1}$$

$$|E_y| = \left|(4 \cdot u \cdot w/\pi\sqrt{\epsilon}) \cdot sin(k \cdot a \cdot v/2) \cdot cosec(k \cdot a \cdot u/2\pi\sqrt{\epsilon})\right| \tag{4.2}$$

Where ϵ is dielectric constant of the dielectric substrate assuming 2.55, a is the diameteter of the antenna assuming 2.75 and k is the wave number calculated as:

$$k = \frac{1.84118}{a\sqrt{\epsilon}} \tag{4.3}$$

For simplicity the constants u, v and w are calculated before the field as:

$$u = sin\theta cos\phi \tag{4.4}$$

$$v = sin\theta sin\phi \tag{4.5}$$

$$w = cos\theta \tag{4.6}$$

The electrical field written following the spherical coordinates are:

$$|E_\theta| = \left|cos(kh \cdot cos\theta)\left(\frac{sin\left(k \cdot \frac{a}{2} \cdot sin\theta sin\phi\right)}{k \cdot \frac{a}{2} \cdot sin\theta sin\phi}\right) cos\left(k \cdot \frac{a}{2} \cdot sin\theta cos\phi\right) cos\phi\right| \tag{4.7}$$

$$|E_\phi| = \left|cos(kh \cdot cos\theta)\left(\frac{sin\left(k \cdot \frac{a}{2} \cdot sin\theta sin\phi\right)}{k \cdot \frac{a}{2} \cdot sin\theta sin\phi}\right) cos\left(k \cdot \frac{a}{2} \cdot sin\theta cos\phi\right) cos\theta sin\phi\right| \tag{4.8}$$

Results of both kind expressions are shown in figures 4.3 and 4.4. The radiation fields are computed and their results shown in the graphics are exactly the same as those proposed by y A. K. Bhattacharjee [15].

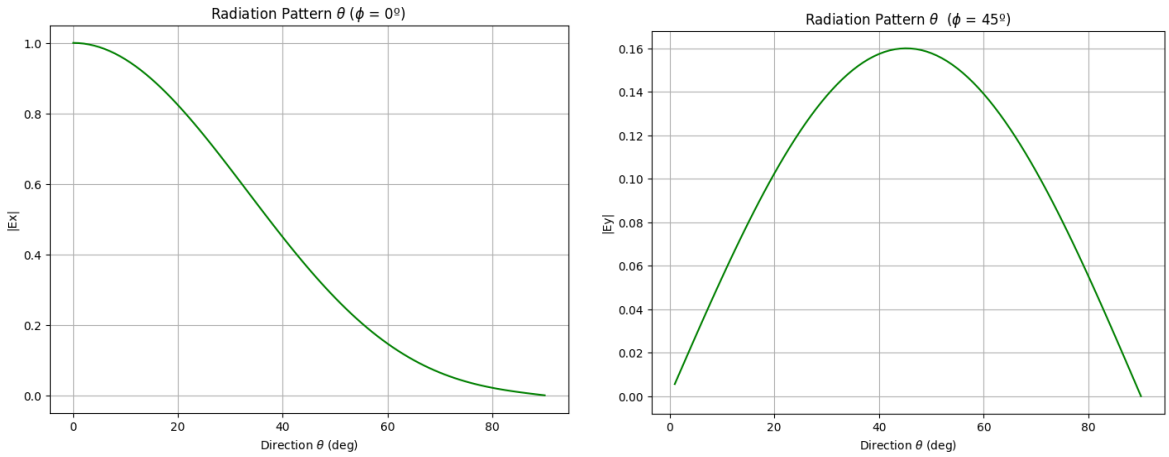

(a) $|E_x|$ versus θ plot for $\phi = 0$ plane.

(b) $|E_y|$ versus θ plot for $\phi = 45$ plane.

Figure 4.3: Rectangular microstrip patch in cartesian coordinates.

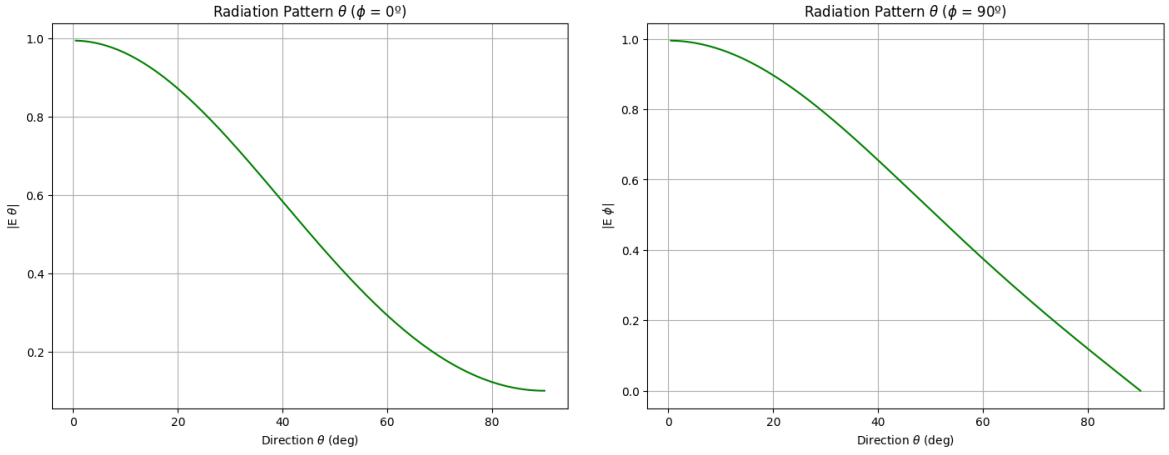

(a) $|E_\theta|$ versus θ plot for $\phi = 0$ plane.

(b) $|E_\phi|$ versus θ plot for $\phi = 90$ plane.

Figure 4.4: Rectangular microstrip patch in spherical coordinates.

4.3.2 Circular Patch

In the case of circular patch, the expresions are modeled in cartesian and spherical coordinates as well as in section before (Rectangular patch). The field expression, according to the cartesian coordinates are:

$$|E_x| = |cos\theta \cdot sinc(kh \cdot cos\theta)\,[J_0(\beta) - cos2\phi J_2(\beta)]| \tag{4.9}$$

$$|E_y| = |cos\theta \cdot sin2\phi \cdot sinc(kh \cdot cos\theta) J_2(\beta)| \tag{4.10}$$

Where h is the thickness of the dielectric substrate assuming $0.01mm$ and β is obtained as:

$$\beta = k(a/2)sin\theta \tag{4.11}$$

The spherical coordinates of far field are estimated as:

$$|E_\theta| = |cos\theta \cdot sinc\,(kh \cdot cos\theta)\,[J_0(\beta) - J_2(\beta)]| \tag{4.12}$$

$$|E_\phi| = |cos\theta \cdot sin\phi \cdot sinc\,(kh \cdot cos\theta)\,[J_0(\beta) + J_2(\beta)]| \tag{4.13}$$

Results of both kind expressions are shown in figures 4.5 and 4.6. The radiation field are computed and their results shown in the graphics are exactly the same as those proposed by A. K. Bhattacharjee et all [15].

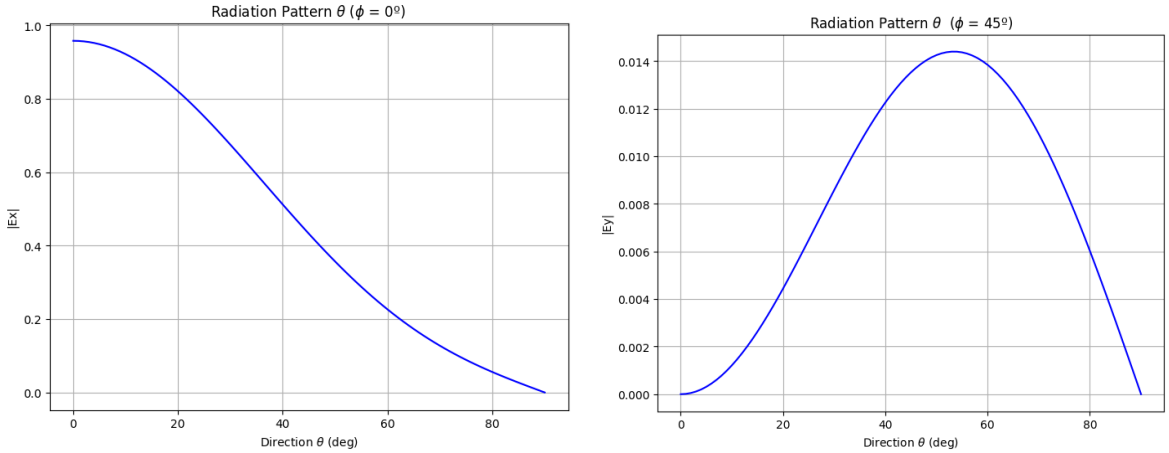

(a) $|E_x|$ versus θ plot for $\phi = 0$ plane.

(b) $|E_y|$ versus θ plot for $\phi = 45$ plane.

Figure 4.5: Circular microstrip patch in cartesian coordinates.

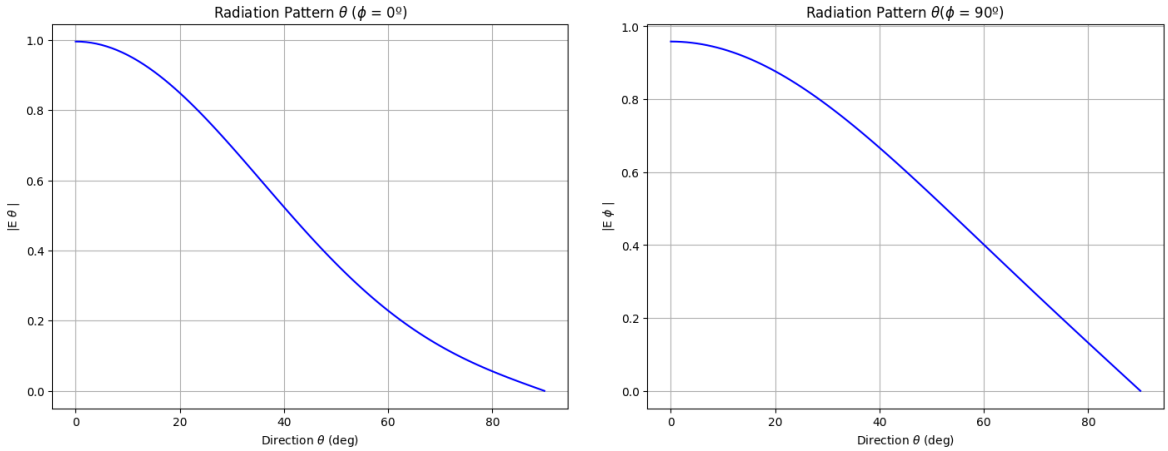

(a) $|E_\theta|$ versus θ plot for $\phi = 0$ plane.

(b) $|E_\phi|$ versus θ plot for $\phi = 90$ plane.

Figure 4.6: Circular microstrip patch in spherical coordinates.

The equations developed for the rectangular and circular patch proposed by A. K. Bhattacharjee et all [15] are useful to compare the shape of the electric field of these patches with those that are going to be designed in a 2D electromagnetic simulator. However, they do not offer gain because they do not include the antenna power parameters. The A. K. Bhattacharjee et all [15] work is based on K. R. Carver and J. W. Mink [16], who uses these same equations taking into account the feeding and design of the patches. The field equations that will be constrasted with the 2D electromagnetic simulator will be the following: first for rectangular patch, and second for circular patch.

$$E_\theta = -\frac{jV_o kae^{-jkr}}{\pi r} \cdot \left(cos(kh \cdot cos\theta) \left(\frac{sin\left(k \cdot \frac{a}{2} \cdot sin\theta sin\phi\right)}{k \cdot \frac{a}{2} \cdot sin\theta sin\phi} \right) cos\left(k \cdot \frac{b}{2} \cdot sin\theta cos\phi\right) cos\phi \right) \tag{4.14}$$

$$E_\phi = \frac{jV_o kae^{-jkr}}{\pi r} \cdot \left(cos(kh \cdot cos\theta) \left(\frac{sin\left(k \cdot \frac{a}{2} \cdot sin\theta sin\phi\right)}{k \cdot \frac{a}{2} \cdot sin\theta sin\phi} \right) cos\left(k \cdot \frac{b}{2} \cdot sin\theta cos\phi\right) cos\theta sin\phi \right) \tag{4.15}$$

$$E_\theta = -\frac{jV_o kae^{-jkr}}{2r} \cdot (cos\theta \cdot sinc\,(kh \cdot cos\theta)\,[J_0(\beta) - J_2(\beta)]) \tag{4.16}$$

$$E_\phi = \frac{jV_o kae^{-jkr}}{2r} \cdot (cos\theta \cdot sin\phi \cdot sinc\,(kh \cdot cos\theta)\,[J_0(\beta) + J_2(\beta)]) \tag{4.17}$$

4.4 CST Design

The electromagnetic field 3D simulation software CST Studio Suite has been employed to design circular and rectangular patch antennas [17]. The main purpose of using this software is to verify that the radiation pattern of the antennas, modeled with the field equations from the paper [15], matches those simulated by the software. In the previous section, it has been shown that the computationally obtained results matches with the results of the paper [15].

Following this procedure, it is guaranteed that the field equations extracted from the literature for rectangular and circular patches are correct. The next step will be to design a rectangular and a circular patch in CST following the specifications of KARFID project. Afterwards, these designs will be transferred to Python to calculate the field equations for those antennas (designed for KARFID).

It is important to note that the main objective of the project consist on the design of software for the study of the radiation patterns of antenna groupings with different configurations. As explained in previous chapters 2.13.

4.4.1 Preliminary patch design

A rectangular patch is designed to compare the similarity between the computational field equations and the CST software simulator, as explained before. This design is based on the equations and the antenna patch proposed by A. K. R. Carver and J. W. Mink [16] following the work of K. Bhattacharjee et all [15]. They proposed using a substrate with a dielectric constant of $\epsilon = 2.5$ and designed the physical dimensions of the patch based on the following graph, which indicates a relationship between the directivity and the radiation edge length, following a function adjusted to the thickness of the substrate.

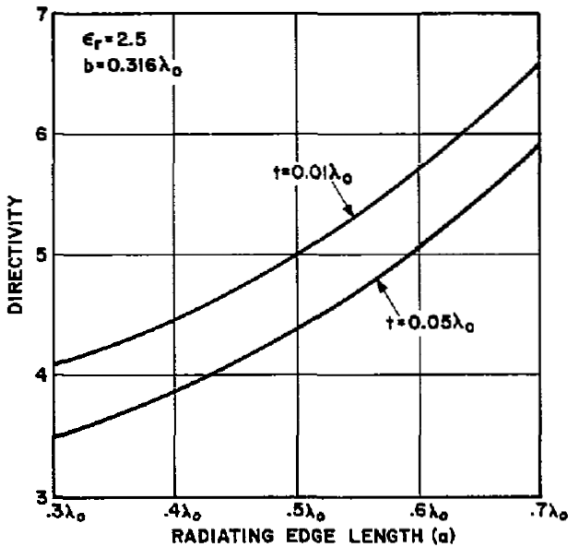

Figure 4.7: Calculated directivity for a rectangular microstrip patch over a large ground plane [16].

In a preliminary desgin the specifications for the rectangular patch were:

- Frequency = 10 GHz
- Patch length = 0.6 λ_0
- Patch width = 0.316 λ_0

- Substrate Thickness = 0.05 λ_0
- Dielectric constant = 2.5

Where λ_0 is the effective wavelength calculated by $\lambda_0 = c/f\sqrt{\epsilon}$.

Once the physical design specifications are established, the process begins by parameterizing the dimensions and designing the patch above the substrate and ground plane.The next step is to feed the patch via a coaxial probe. The coaxial probe will be in contact with the bottom of the patch, crossing an intersection in the ground plane and the substrate. It is important to determine the feeding point to obtain an impedance of 50 Ω. It is known that the current intensity is maximum at the center of the patch, while the voltage is minimum at the center and maximum at the edges of the patch. Therefore, to obtain an impedance matched at 50 Ω, the feeding point is calculated using these equations [18]:

$$R_{in} = R_0 cos^2\left(\frac{\pi L_1}{L}\right) \tag{4.18}$$

$$R_0 = \frac{\eta_0 \lambda_0}{2\pi W\left(1 - \frac{1}{6}\left(\frac{\pi h}{\lambda_0}\right)^2\right)} \tag{4.19}$$

Here, R_{in} represents the impedance at 50 Ω, and L_1 is the distance from the edge of the patch to place the feed point. CST has a tool that allows the calculation of the impedance of the coaxial probe from the exterior and interior diameters and the electric permittivity of the dielectric. The coaxial probe is composed of external conductor, electric substrate (Teflon with dielectric constant $\epsilon_r = 2.2$), and internal conductor.

After positioning the coaxial probe at the optimal point, boundary conditions are specified. All of the surrounding planes except for the botom are configurated as open (add space), which allow waves to exit the simulation domain, whithout reflecting back, thus behaving as an infinite-like environment and enabling accurate far-field simulations. In the lower face, the tangential component of the electric field is set to zero, which resembles the surface of PEC (perfect electric conductor). Therefore the lower boundary acts as an infinite ground plane [19].

To simulate the far field, the time-domain solver is selected, as it best suits the type of structure to be simulated. It utilizes hexaedral meshing simulador. A plane of symmetry in the XZ plane, where the tangential magnetic field is zero, is used. Finally, a waveguide port is placed at the coaxial probe face.

With this preliminary design based on theoretical data, several simulations were conducted, modifying the length of the patch and feeding position until the S11 parameter reaches a minimum at the central frequency of 10 GHz. The optimized dimensions fot the patch length and width are $0.6\lambda_0$ and

$0.44\lambda_0$. With these new dimensions, the far field is monitored, and field pattern cuts are taken to compare with Python.

This process was repeated for the circular patch, with final dimensions equal to the rectangular one, except for the radius, which is $r = (0.315 \cdot \lambda)/2$.

Figures 4.8 and 4.9 represent the main cuts normalized in $\phi = 0^{\text{o}}$ and $\phi = 90^{\text{o}}$. In both field comparisons between the CST experimental model and the computational model in Python, it is observed that the alignment is highly accurate. The behavior of the field exhibits consistent trends. Thus, demonstrating the validity of the antenna field equations for the project.

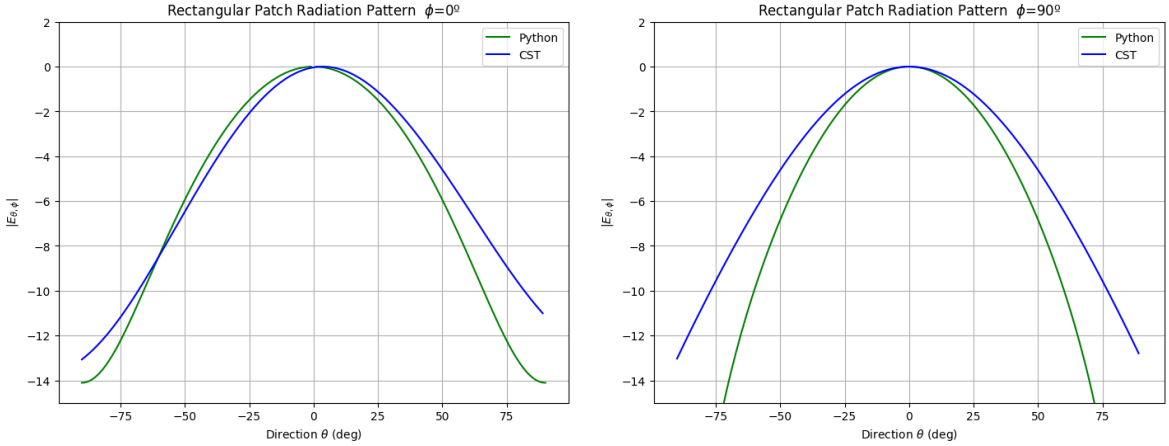

(a) $|E_\theta|$ versus θ plot for $\phi = 0$ plane. (b) $|E_\theta|$ versus θ plot for $\phi = 90$ plane.

Figure 4.8: Rectangular patch microstrip patch preliminary design.

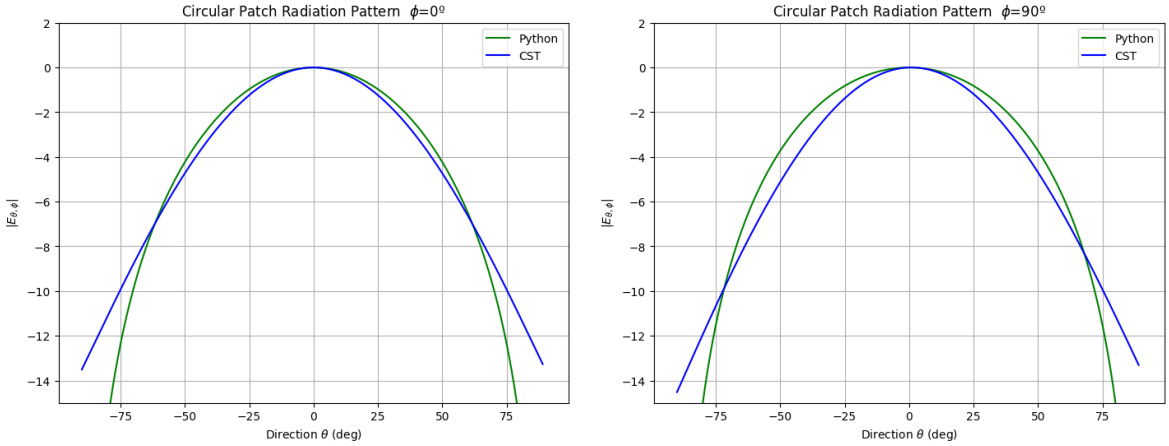

(a) $|E_\theta|$ versus θ plot for $\phi = 0$ plane. (b) $|E_\theta|$ versus θ plot for $\phi = 90$ plane.

Figure 4.9: Circular patch microstrip patch preliminary design.

4.4.2 Patch design

In this section, a patch that satisfies KARFID specifications is going to be designed:

- Frequency = 30 GHz
- Substrate =RO3035
- Loss Tangent = 0.0015
- Substrate thickness = 0.05 mm
- Dielectric constant = 3.6

A process similar to the preliminary design phase has been followed to model these structures. The data has been parameterized for the design of the different parts of the patch. The patch feed point has been optimized following the equations 4.18 and 4.19. The boundary conditions are still open and adding extra space and the selected simulator is again a time domain solver.

Several simulations were conducted, sweeping frequencies from 25 GHz to 35 GHz, with the center frequency at 30 GHz. The physical dimensions of the patch and the feeding point were modified in various simulations until the S11 parameter reached its minimum at the center frequency, where the structure was well matched at the center frequency. The final physical dimensions for the square patch are a length of 2.2 mm, and for the circular patch, a radius of 1.35 mm.

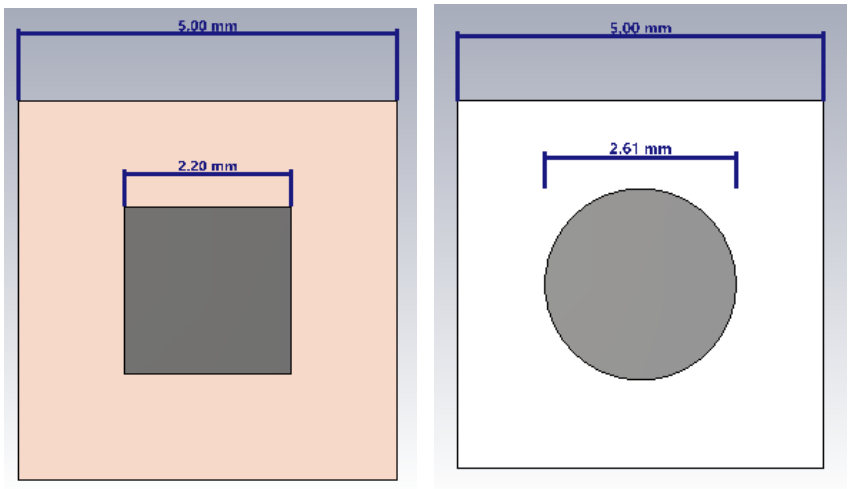

Figure 4.10: Front of view square patch design (left) and circular patch design (right).

Then, a far field monitor is configured at the center frequency to observe the radiation patterns. The normalized main cuts are exported to be compared with the ones, calculated usign the Python software. The inputs for the Python field equations have been adjusted to obtain the new radiation patterns for the KARFID circular and square patch.

Figures 4.11 and 4.12 display the normalized main cuts of the radiation patterns for both the CST and Python simulation results. It is worth noting that in this case, the alignment is significantly better than in the preliminary design.

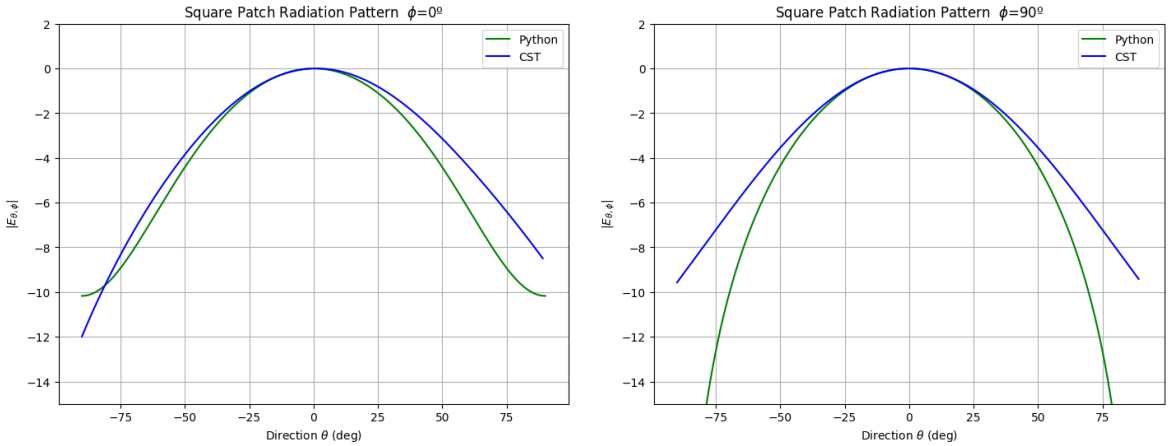

(a) $|E_\theta|$ versus θ plot for $\phi = 0$ plane.

(b) $|E_\theta|$ versus θ plot for $\phi = 90$ plane.

Figure 4.11: Square patch microstrip patch KARFID design.

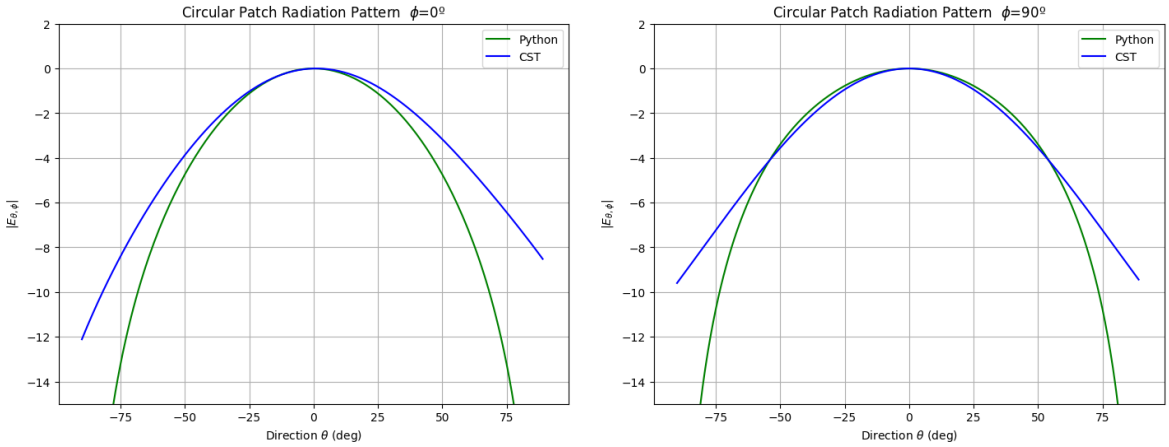

(a) $|E_\theta|$ versus θ plot for $\phi = 0$ plane.

(b) $|E_\theta|$ versus θ plot for $\phi = 90$ plane.

Figure 4.12: Circular patch microstrip patch KARFID design.

Chapter 5

Array Analysis Of Different Configurations

In this chapter, various configurations of antenna arrays evaluated in this project are presented. This includes the mathematical model implemented in Python and the designs developed in CST to verify their proper functionality. Additionally, a comparative analysis between the theoretical models and the simulation results is discussed. This comprehensive approach ensures robust validation of the antenna designs within the specified frequency range.

5.1 Linear Array

The linear array structure was presented in Section 2.3, where it is explained that antennas are arranged in a row or a column, as shown in Figure 5.1. In the previous section, the structure of an array factor was explained to demonstrate how the arrangement of antennas and the dependence on the number of antennas can widen the main lobe. Additionally, it illustrates how the progressive increase in phase achieves a translation of the main lobe to point in the desired direction, albeit with a reduction in gain compared to broadside pointing. The linear array factor equation modeling this behavior was also presented.

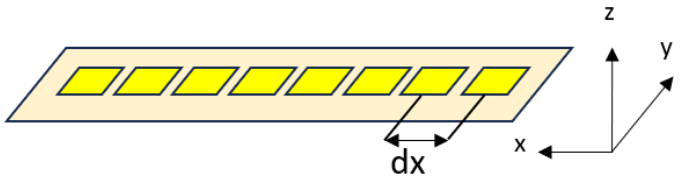

Figure 5.1: Example distribution linear array ($N = 8$).

$$AF = \sum_{n=1}^{N} \frac{I}{\sqrt{N}} e^{j(n-1)\cdot kd(cos\theta + cos\theta_o)} \tag{5.1}$$

In the previous chapter, the field equations of the microstrip patches were developed both computationally and through simulation in CST. Now, it is time to model the radiation pattern of the antenna distributions. It is known that the radiation pattern of an antenna configuration, assuming all antennas are equal, is the field equation of the individual antenna multiplied by the array factor, as stated in Equation 2.13. A linear array of 8x1 along the x-axis, similar to the one in Figure 5.1, was evaluated. The distance between the patches will be 0.5λ, and a uniform distribution with an amplitude of 1 for each element will be considered.

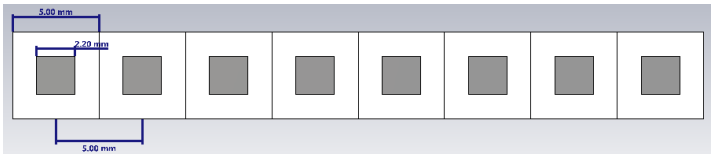

Figure 5.2: Front of view linear array distribution of square patch desgin ($N = 8$).

In the CST simulation environment, the initial design of the individual patch is based on the KARFID specifications. The array factor is applied to this design, specifying the distances between patches (0.5λ), the amplitude of each antenna (1 for all elements), and a progressive phase for pointing. The configuration is shown in Figure 5.2. It should be noted that an 8x1 patch configuration has not been specifically evaluated; instead, the array factor has been applied to a single patch to reduce the simulation and meshing time of the structure in CST. This has been also considered in the following configurations. Therefore, the represented far fields are not actual whole array simulation results, but an array factor applied to a single patch, as it can see in Figure 5.3.

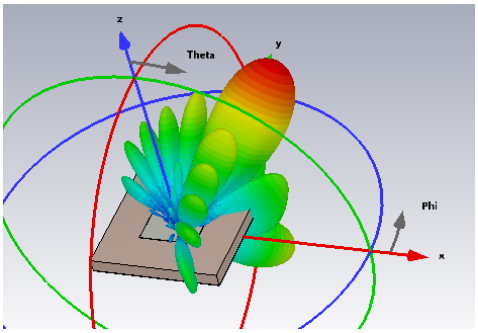

Figure 5.3: Farfield ilustration, an array factor applied over a patch.

In Python, the field equations of the patches, sized according to the KARFID project, have been implemented and multiplied by the array factor according to equation 5.1. This setup has been designed

to compare the evaluated radiation pattern in python and CST in the two main planes. At $\theta = 0^{o}$ and $\theta = 30^{o}$, with the normalized cuts represented in Figures 5.4 and 5.5.

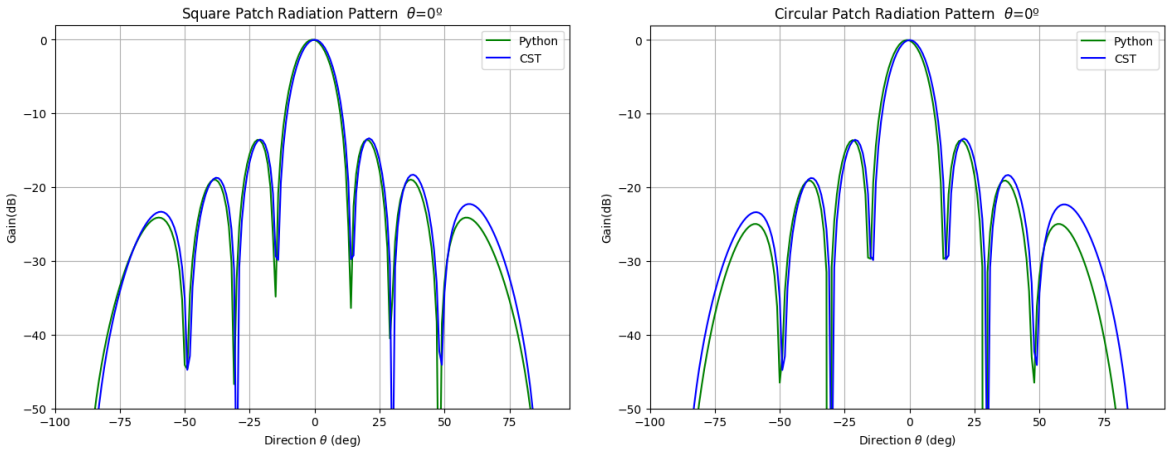

Figure 5.4: Radiation pattern of an 8 element linear array pointing broadside (left figure for square patch, right figure for circular patch).

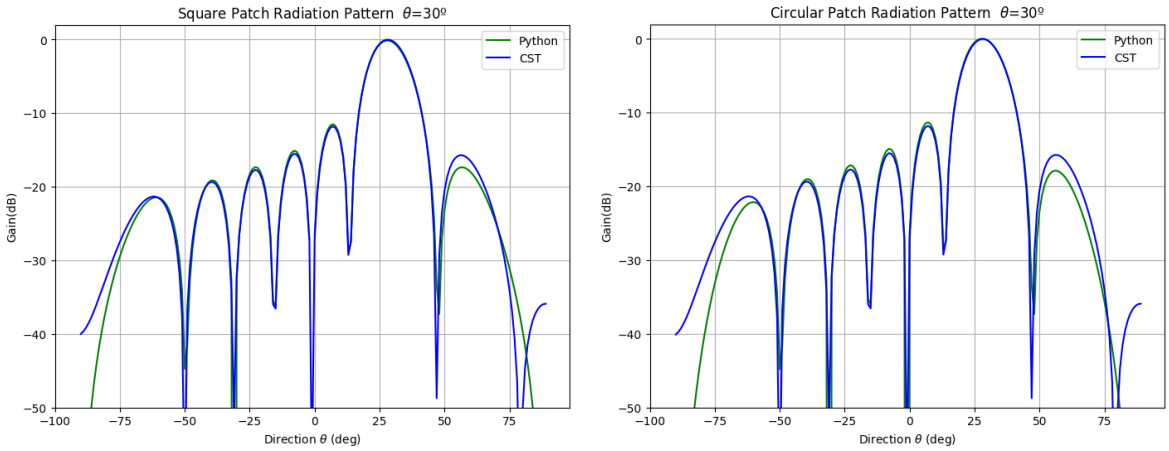

Figure 5.5: Radiation pattern of an 8 element linear array pointing $\theta = 30^{o}$(left figure for square patch, right figure for circular patch).

5.2 Planar Array

A planar array is a structure where antennas are positioned along a surface. When the feeding amplitude and phase of element is tunable. It is useful for scan radar, the main beam can be steered towards any point in space. The array factor of a planar array considers two axes, making it necessary to account for progressive phases, amplitudes, and distances between elements in both axes.

5.2.1 Regular Planar Array

Regular arrays position their antennas along a rectangular grid (shown in Figure 5.6). In this work, distance between elements of a certain direction is kept constant but dx can be different from dy.

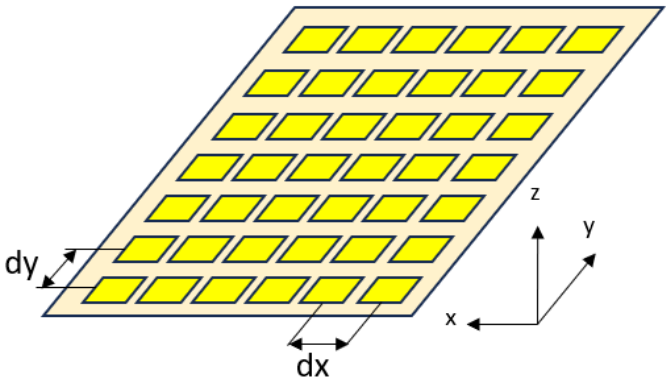

Figure 5.6: Example planar array ($N = 7$ and $M = 6$).

Suppose a planar array above the X-Y plane, with N elements along the y-axis and M elements along the x-axis, as shown in Figure 5.6. The equation can be written as:

$$AF = \sum_{n=1}^{N} \frac{I_n}{\sqrt{N}} \left[\sum_{m=1}^{M} \frac{I_m}{\sqrt{M}} e^{j(m-1)(kd_x sin\theta cos\phi + \beta_x)} \right] e^{j(n-1)(kd_y sin\theta \sin\phi + \beta_y)} \tag{5.2}$$

where d_x and d_y represent the distances between radiating elements in the x and y directions. To prevent grating lobes, as explained previously, the optimal distance must be $\lambda/2$. Similarly, β_x and β_y are the progressive phases, independent to each other, and adjust the beam to the maximum of the main beam at desired angle to point to $\theta = \theta_o$ and $\phi = \phi_o$, so the phase shifts are expressed as:

$$\beta_x = -kd_x sin\theta_o cos\phi_o \tag{5.3}$$

$$\beta_y = -kd_y sin\theta_o sin\phi_o \tag{5.4}$$

Finally, I_m and I_n are the excitation coefficients of each element. If the amplitude excitation of the entire array is uniform, it is , $I_o = I_m = I_n$.

Figure 5.7 illustrates a three-dimensional pattern of 8x8 elements pointing to $\theta_o = 0^o$ and ϕ_o=0^o, with the distance between elements equal to $d_x = d_y = \lambda/2$. The antennas are identical and present the same amplitude.

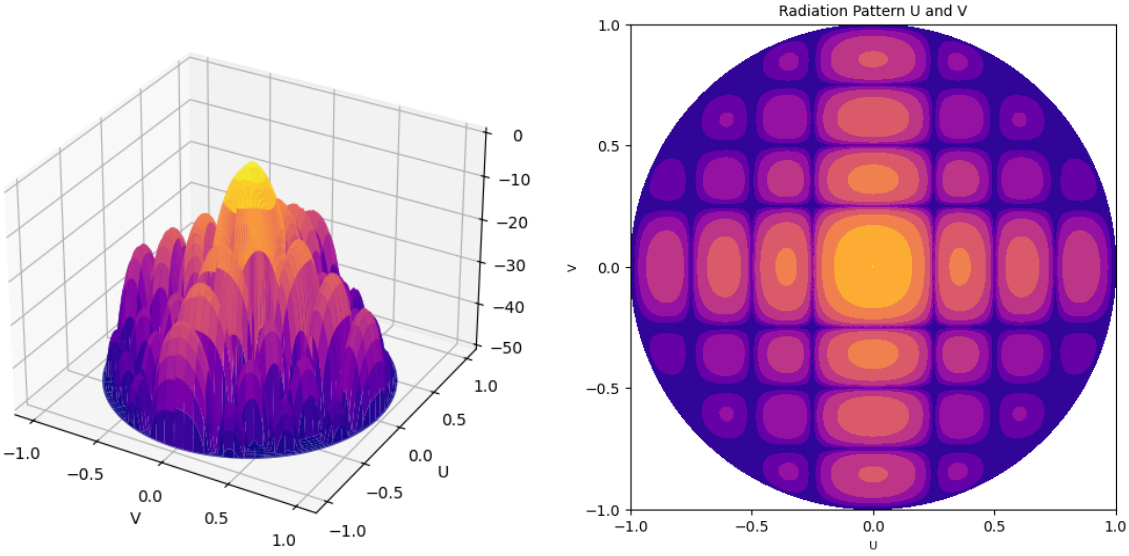

Figure 5.7: Example regular planar array $N = M = 8$ elements with distance between elements of $dx = dy = \lambda/2$ and equal amplitude and phase.

In CST, a regular planar array with a distribution of 8x8 was modeled, assuming a uniform amplitude of 1 for each element, and a distance between each patch in the x-axis and y-axis equal to 0.5λ. A uniform distribution equal to 1 is assumed because this type of feed is simpler to handle and generates a narrow beam, although with high sidelobes. There are other forms of feed distribution, such as binomial or tapering, which can be used to control both the beamwidth and the SLL. This configuration is shown in Figure 5.8. This planar array was modeled to point in different directions, specifically: first broadside, second $\theta = 30^o$, third $\phi = 15^o$, $\theta = 20^o$, $\phi = 30^o$ and fourth $\theta = 45^o$, $\phi = 45^o$. To achieve these desired directions, the progressive phases were calculated for each case and input into the CST environment. Then, the field pattern cuts were compared with the computational model, as shown in Figures 5.9 and 5.10.

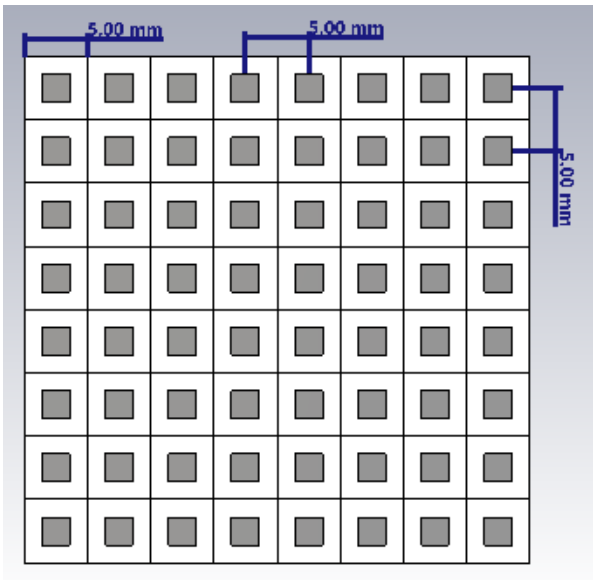

Figure 5.8: Front of view regular planar array distribution of square patch ($N = M = 8$).

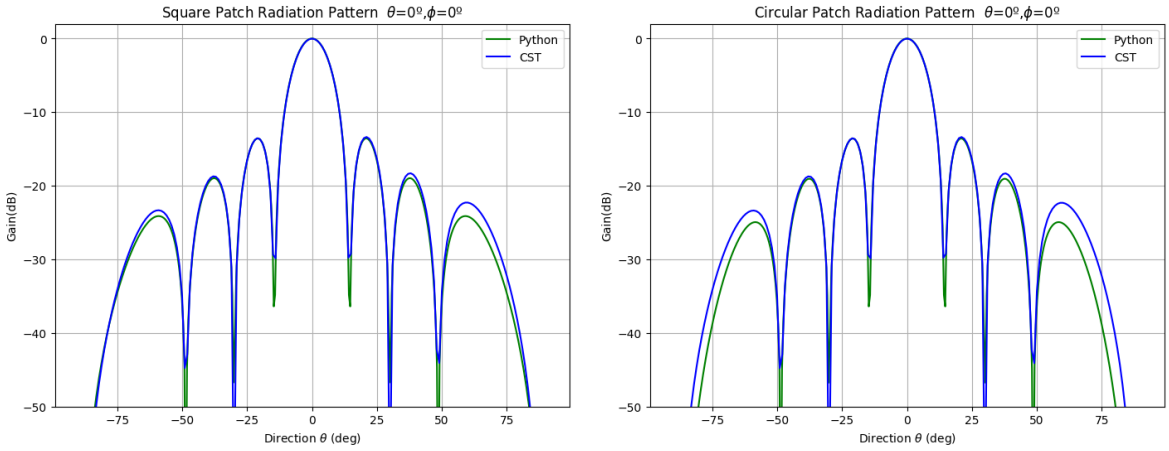

Figure 5.9: Radiation pattern of an 8x8 elements regular planar array pointing broadside (left figure for square patch, right figure for circular patch).

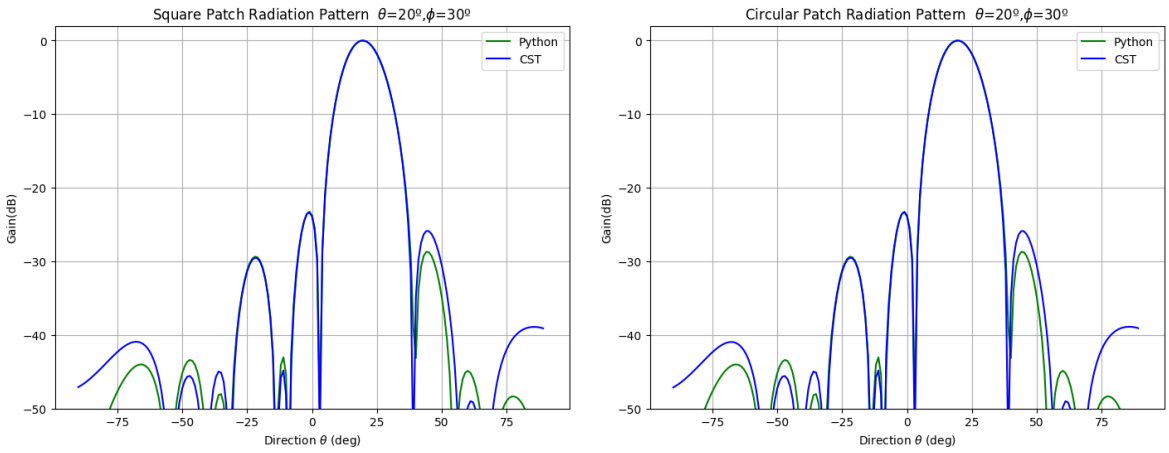

Figure 5.10: Radiation pattern of an 8x8 elements regular planar array pointing $\theta = 30^{o}$ and $\phi = 20^{o}$ (left figure for square patch, right figure for circular patch).

5.2.2 Shifted Array

A shifted array is a planar structure similar to a regular structure, with elements along both axes, where the main difference lies in the antenna distribution; in this case, the antennas are regulary placed along one axis, as in the regular structure, but interleaved along the other axis (shown in Figure 5.11).

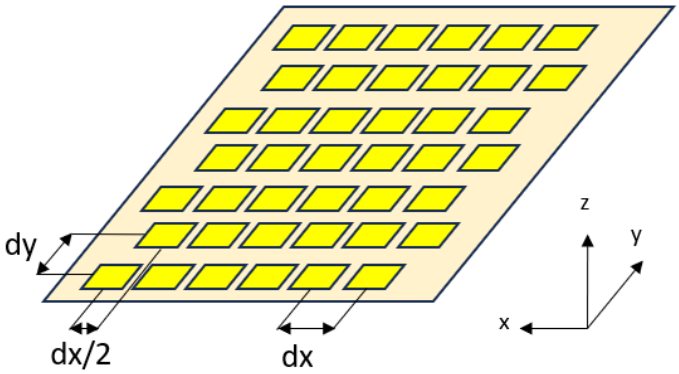

Figure 5.11: Example shifted planar array ($N = 7$ and $M = 6$), intercallar scroll along x axis $dx/2$.

The mathematical equation that describes the shifted array factor is the same as that for the regular array factor:

$$AF = \sum_{n=1}^{N} \frac{I_n}{\sqrt{N}} \left[\sum_{m=1}^{M} \frac{I_m}{\sqrt{M}} e^{j(m-1)(kd_x sin\theta cos\phi + \beta_x)} \right] e^{j(n-1)(kd_y sin\theta \sin\phi + \beta_y)} \tag{5.5}$$

The distinction lies in the varying distances between elements along one of the axes. Implementing this equation without any changes will yield the same results as a regular array. Therefore, it is necessary to construct a matrix with the positions of each element, considering the initial positioning of

the first element on the coordinate axis as the reference point for the progressive offset. The parameters dx and dy indicate the distances between the elements on the x and y axes, respectively, while the subscripts m and n indicate the progressive phase difference with respect to the first element. To construct the matrix of array positions, the distances between elements, the subscripts, and the offset for interleaving along one of the axes must be taken into account. For example, in a 4x4 distribution with a $\lambda/4$ offset:

n/m	0	1	2	3
0	0 , 0	0 , dy	0 , $2dy$	0 , $3dy$
1	dx , $dy \cdot \frac{1}{2}$	dx , $dy + dy \cdot \frac{1}{2}$	dx , $2dy + dy \cdot \frac{1}{2}$	dx , $3dy + dy \cdot \frac{1}{2}$
2	$2dx$, 0	$2dx$, dy	$2dx$, $2dy$	$2dx$, $3dy$
3	$3dx$, $dy \cdot \frac{1}{2}$	$3dx$, $dy + dy \cdot \frac{1}{2}$	$3dx$, $2dy + dy \cdot \frac{1}{2}$	$3dx$, $3dy + dy \cdot \frac{1}{2}$

Table 5.1: Matrix of the positions of the 4x4 array with offset $\lambda/4$ along y-axis.

n/m	0	1	2	3
0	0 , 0	dx , 0	$2dx$, 0	$3dx$, 0
1	$dx \cdot \frac{1}{2}$, dy	$dx + dx \cdot \frac{1}{2}$, dy	$2dx + dx \cdot \frac{1}{2}$, dy	$3dx + dx \cdot \frac{1}{2}$, dy
2	0 , $2dy$	dx , $2dy$	$2dx$, $2dy$	$3dx$, $2dy$
3	$dx \cdot \frac{1}{2}$, $3dy$	$dx + dx \cdot \frac{1}{2}$, $3dy$	$2dx + dx \cdot \frac{1}{2}$, $3dy$	$3dx + dx \cdot \frac{1}{2}$, $3dy$

Table 5.2: Matrix of the positions of the 4x4 array with offset $\lambda/4$ along x-axis.

Now, the equation is remodeled as follows:

$$dx = matrix[m-1][n-1][0] \tag{5.6}$$

$$dy = matrix[m-1][n-1][1] \tag{5.7}$$

$$AF = \sum_{n=1}^{N} \frac{I_n}{\sqrt{N}} \left[\sum_{m=1}^{M} \frac{I_m}{\sqrt{M}} e^{j(kd_x sin\theta cos\phi + \beta_x)} \right] e^{j(kd_y sin\theta \sin\phi + \beta_y)} \tag{5.8}$$

Figure 5.12 illustrates a three-dimensional pattern of 8x8 elements pointing to $\theta = 0^{o}$ and $\phi = 0^{o}$, with the distances between elements equal to $dx = dy = /2$ and a scroll offset of $\lambda/4$. The antennas are identical and present the same amplitude.

In comparison with a regular planar array, the main lobe and the sidelobe level (SLL) of the shifted array are quite similar in both structures. Additionally, the advantage of the shifted structure is that it provides a radiation pattern with lower side lobes, as seen in Figure 5.13. The shifted structure can

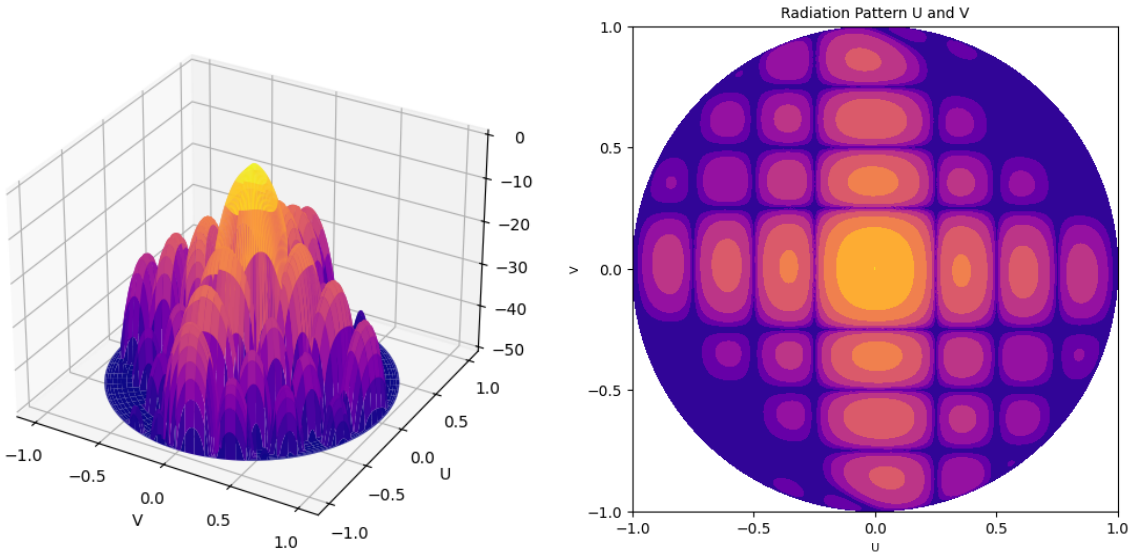

Figure 5.12: Example shifted planar array $N = M = 8$ elemnts with distance between elements $dx = dy = \lambda/2$ and scroll offset $\lambda/4$, and equal amplitude an phase.

introduce asymmetries in the radiation pattern, depending on the value and direction of the applied phase shift.

The same cases as in the regular planar array section have been modeled in CST, introducing an interleaved offset shift of $\lambda/4$ in the x-axis (see Figure 5.14). The maximum gain in the shifted array is the same as in the regular array. The main lobe also maintains the same beam width, as shown in Figures 5.15 and 5.16. The Side Lobe Level (SLL) remains at the same level as in the regular case, but the secondary lobes start to appear more than 50 dB below the maximum peak gain, making the signal negligible at that point.

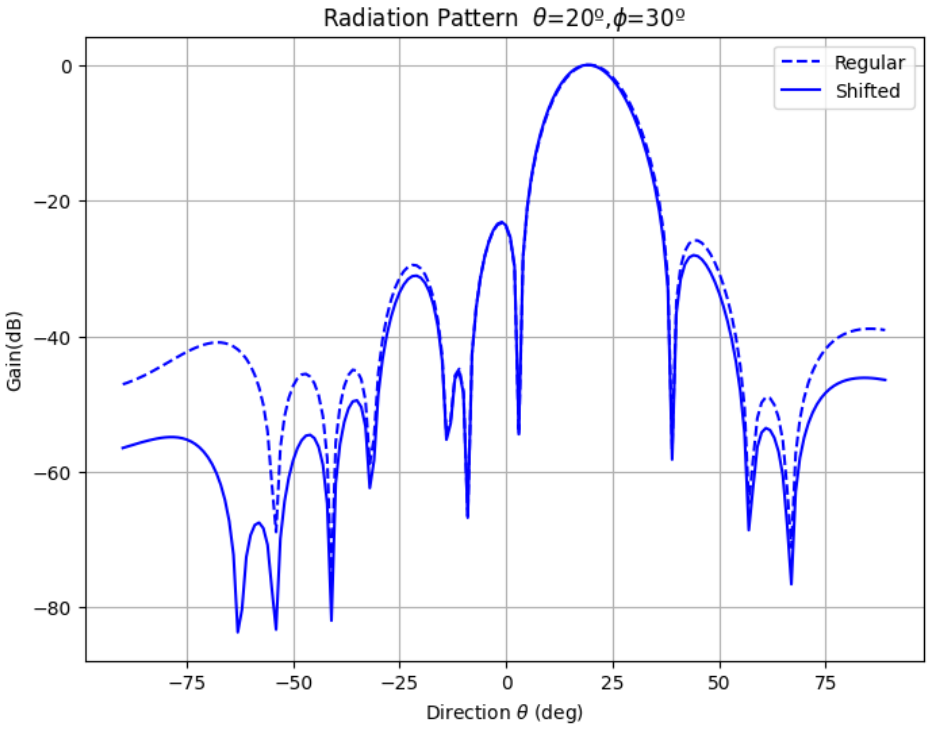

Figure 5.13: Example shifted and regular planar array ($N = 8$ and $M = 8$).

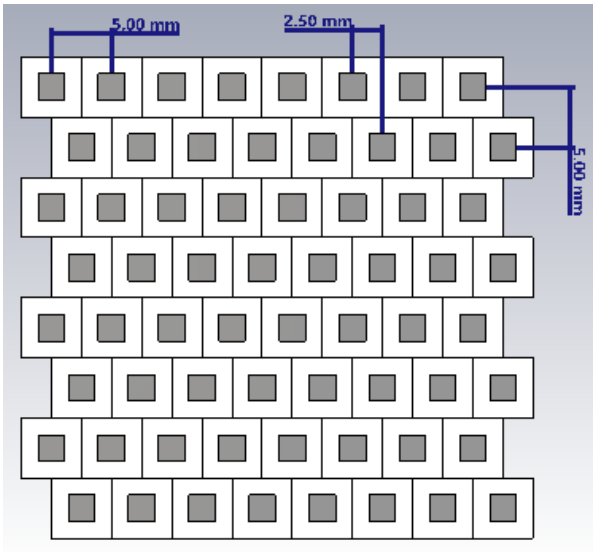

Figure 5.14: Front of view shifted planar array distribution of square patch ($N = 8$ and $M = 8$).

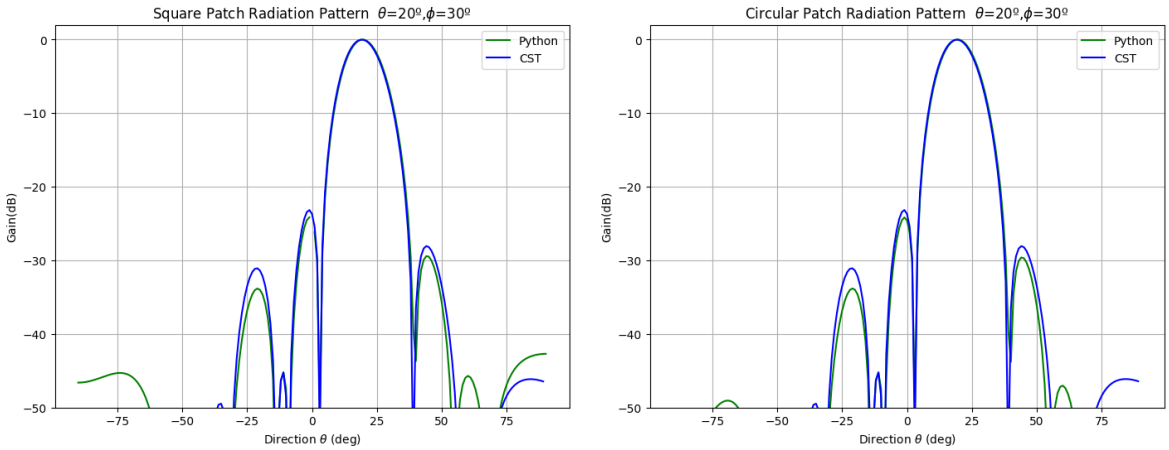

Figure 5.15: Radiation pattern of an 8x8 elements shifted planar array pointing $\theta = 20^{o}$ $\phi = 30^{o}$.

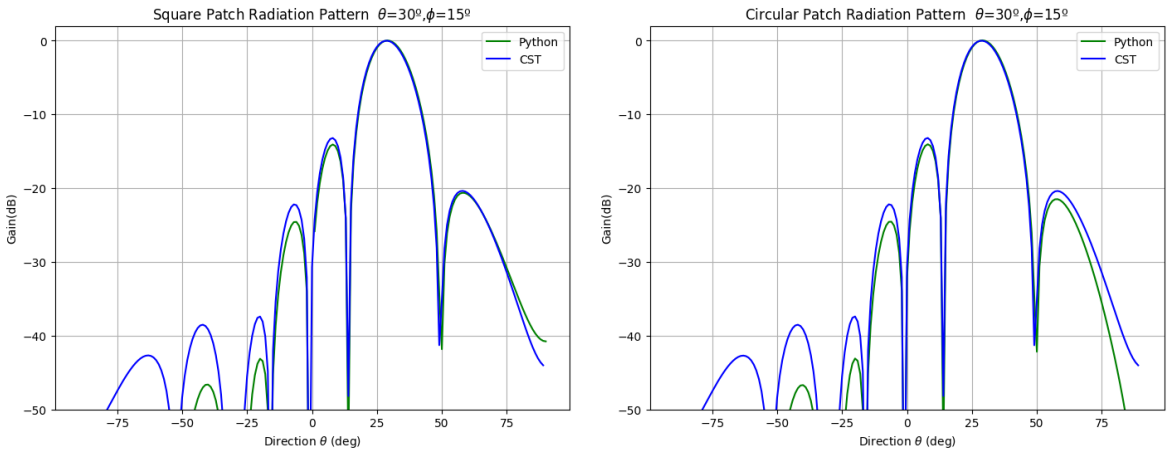

Figure 5.16: Radiation pattern of an 8x8 elements shifted planar array pointing $\theta = 30^{o}$ $\phi = 15^{o}$.

5.3 Ring Array

Ring array structure consists of situated the radiating elements around a point, with a circular arrangement, as shown in Figure 5.17. It is a useful structure for a small antenna configuration capable to point in elevation and azimuth. The ring array factor equation modelig is presented [20]:

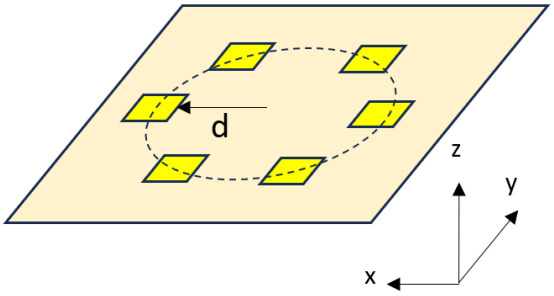

Figure 5.17: Example distribution ring array ($N = 6$).

$$AF = \sum_{n=1}^{N} \frac{I}{\sqrt{N}} e^{j \cdot kd(sin\theta cos(\phi - \phi_n) + \beta_n)} \tag{5.9}$$

Where d now is the radius of the circular ring insted of the distance between the elements, ϕ_n is the angular position of the n^{th} element which is expresed as $\phi_n = 2\pi\,(n/N)$. And finally, β_n is the phase excitation of the n^{th} element. To steer the main lobe in the $theta_0$ and ϕ_0 the phase excitation of th n^{th} element can be chosen to be:

$$\beta_n = -kd \cdot sin\theta_0 cos\,(\phi_0 - \phi_n) \tag{5.10}$$

The progressive phase is calculated asuming the center of the ring the origin of coordenates. Figure 5.18 show a example of three-dimensional pattern of 6 elements potinting to $\theta = 0^{\text{o}}$ and $\phi = 0^{\text{o}}$ with a distance respect center of the ring equals to $d = 0.5\lambda$. The antennas are identical and present the same amplitude.

In CST a ring array with 6 elements was developed, assuming a distance respect the center equal to 0.5λ. This array was modeled to point in to broadside and $\theta = 20^{\text{o}}$ $\phi = 30^{\text{o}}$. Following a similar process as the other antennas configuration was compare the computational model with the simulation model as shown in Figure 5.19. The ring array has a main lobe with a very wide bandwidth, it is a non-directive main lobe, with very high secondary lobe separation. The advantage of this topology is that fewer antennas are used but at the cost of much more complicated integration in real systems.

It has been compared in python graphs that the behavior of a ring modeled with the previous expression and with the expression of the regular array factor modeled as a function of the x and y

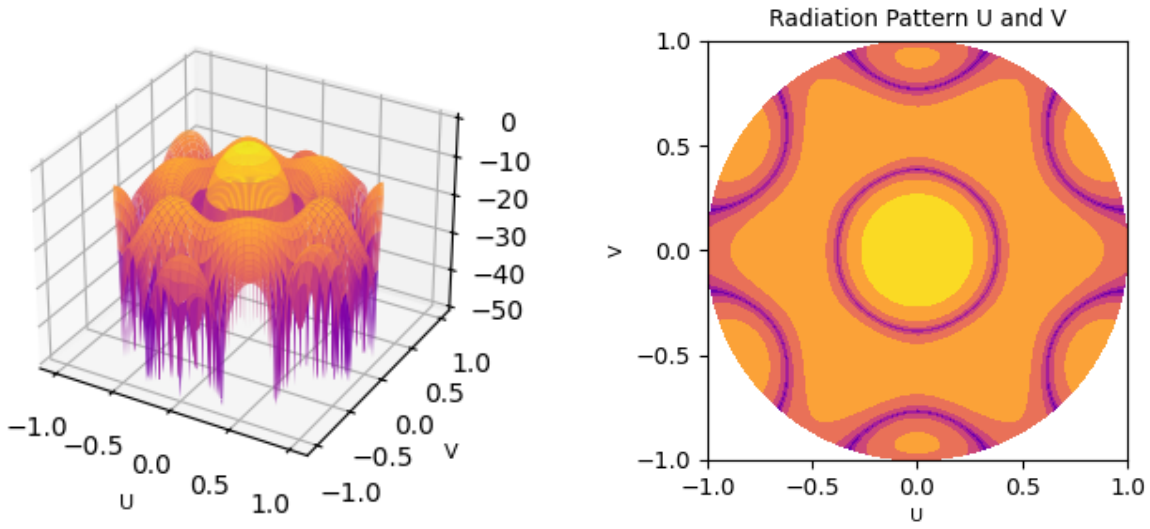

Figure 5.18: Example ring array $N = 6$ elements with distance respect the center $d = \lambda/2$.

positions of the radiating elements, acting as if we had an array in cells but with unlit patches and only those that form a circle transmitted. It was verified that both equations return the same results.

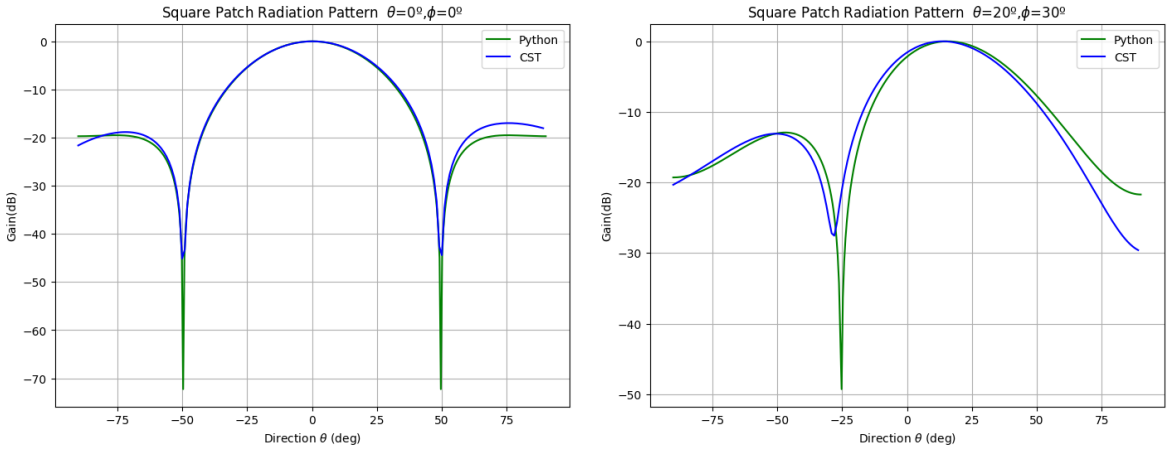

Figure 5.19: Radiation pattern of an $N = 6$ square elements ring array.

5.3.1 Concentric Array

A concentric array is a quite similar strucure as ring array, but in this case another patch is located at the center of the ring, as it can see in Figure 5.20.

The concentric array factor equation modelig is the ring array factor equation presented before introducing a change [20]:

$$AF = e^{j\beta_x} + \sum_{n=1}^{N} \frac{I}{\sqrt{N}} e^{j \cdot kd(sin\theta cos(\phi - \phi_n) + \beta_n)} \tag{5.11}$$

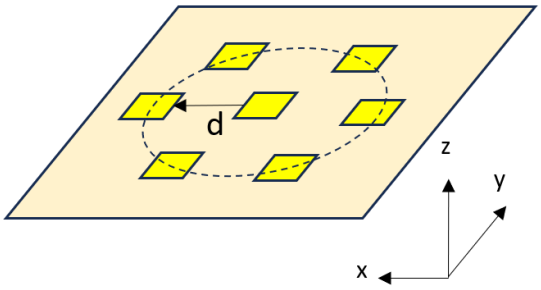

Figure 5.20: Example distribution concentric array ($N = 7$).

The component $e^{j\beta_x}$ represents the first component situated in the center and assuming that this point is the origin of coordenates. Where β_x is the phase excitation of the element at the center. Normally in the summation we start counting from 1 to N and the superscripts of the exponent are n-1, then the first component has the exponent at 0 regardless of the pointing direction and therefore its value is its amplitude, which is considered amplitude. equal to 1 for all, the first element to add to the array is 1. Thus that, is considerate $e^{j\beta_x} = 1$.

A distribution of 6 square antennas positioned in a ring plus one additional element located at the center of the ring, with a distance of 0.5λ from the rest of the elements is set. This distribution has been computationally modeled with the expression of the concentric array factor and with the regular array factor. In this model, it has been considered as if the antennas were placed in cells and their adjacent ones were turned off. Ideally, with the positions of the antennas turned on, it should present a radiation pattern equal to the concentric array factor. Figure 5.21 shows the radiation pattern of this configuration antennas with a broadside pointing. The results from CST do not match those described by [20], so this approximation method was discarded and will be evaluated based on the following case study.

The main idea of concentric structure is to improve the topology of the ring by adding one more element that adds gain to the radiation pattern, and reduces the SLL and the appearance of the null, simply adding one more element in the center but with an ideal distance of 0.5λ represents a significant change in the radiation pattern as can be seen in Figure 5.22.

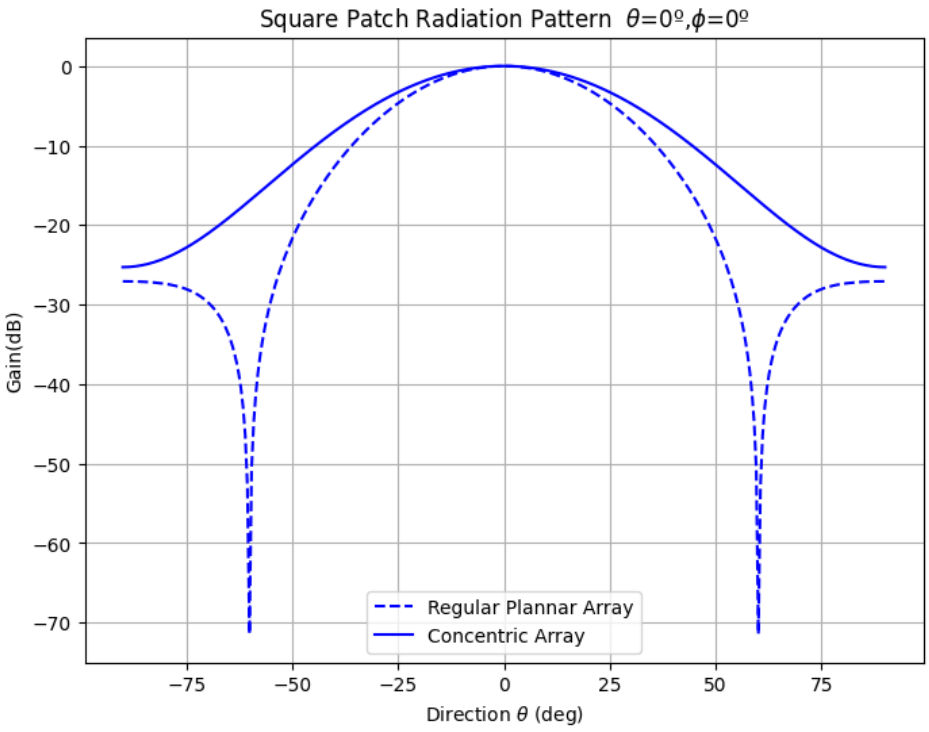

Figure 5.21: Example regular and concentric array ($N = 7$).

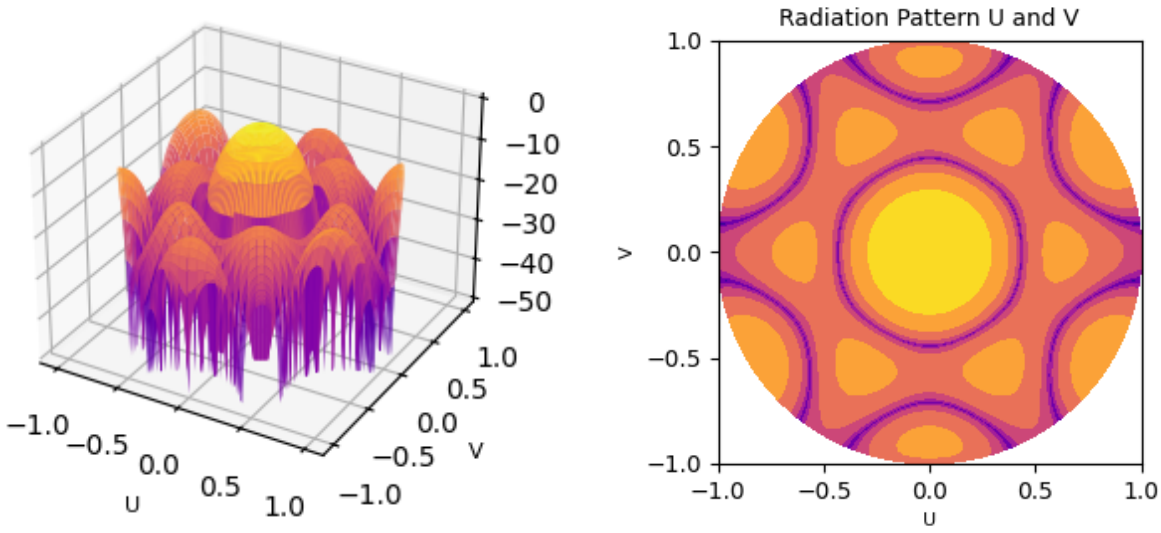

Figure 5.22: Example concentric array $N = 7$ elements with distance respect the center $d = \lambda/2$.

5.4 Random Array

Those groupings that do not follow a canonical distribution must be evaluated based on the unit contribution of the elements that compose it regardless of their relative position or their feeding properties.

For this purpose, in this master's final project the random array evaluation functionality is added based on the description contained in a data file with the following structure, positions in three axis, amplitude and phase, see Table 5.3:

Position X	Position Y	Position Z	Amplitude	Phase
0	0	0	1	0
$\lambda/2$	0	0	1	-0.931
$\lambda/2 \cdot 1/2$	$\lambda/2 \cdot \sqrt{3}$	0	1	-0.931
$-\lambda/2 \cdot 1/2$	$\lambda/2 \cdot \sqrt{3}$	0	1	0
$-\lambda/2$	0	0	1	0.931
$-\lambda/2 \cdot 1/2$	$-\lambda/2 \cdot \sqrt{3}$	0	1	0.931
$\lambda/2 \cdot 1/2$	$-\lambda/2 \cdot \sqrt{3}$	0	1	0

Table 5.3: Example structure data file

The example shown in Table 5.3 is from the previous section; 7 square antennas in a concentric array, with a radius from the central element of 0.5λ and pointing to $\theta_0 = 20^{\text{o}}$ $\phi = 30^{\text{o}}$. This example serves as a test of the similarity between CST and the code developed in Python, as shown in Figure 5.23

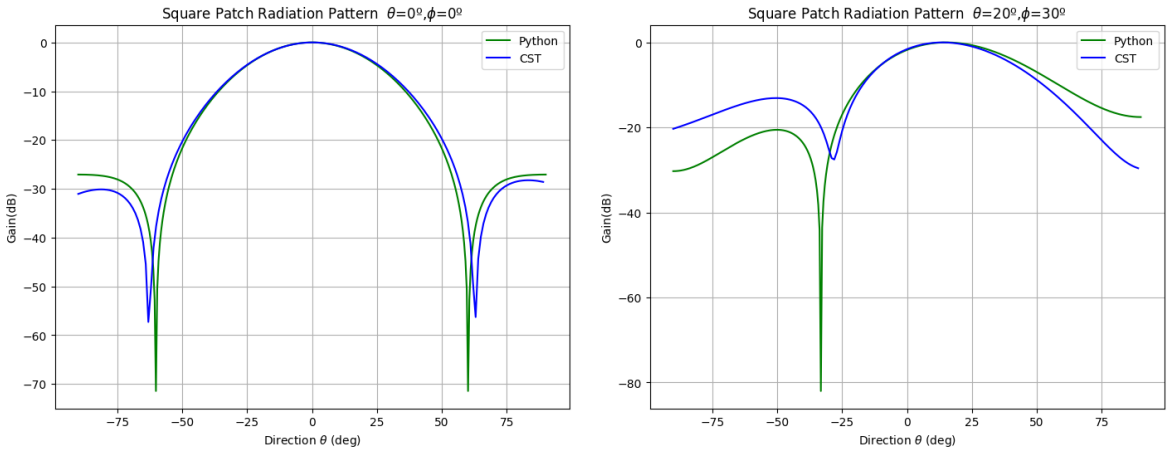

Figure 5.23: Radiation pattern of an $N = 7$ square elements random array.

Chapter 6

Software Development

This chapter will explain step by step how the graphical interface has been developed for the study of the radiation patterns of the different types of antenna configurations. The software has been developed in Python from libraries such as tkinter and pyqt5 used for the design of graphical interfaces. As design support in the aesthetic part of location and localization of widgets, the tool that has been selected was QtDesigner.

6.1 Used Tools

In developing the graphical interface for studying the radiation patterns of different antenna configurations, Python has been used as the programming language. Python is an open-source language widely used by the scientific community due to its extensive range of libraries and specialized tools that facilitate the development of scientific and engineering applications.

Tkinter is the primary library in Python for developing graphical interfaces [21]. However, the interfaces that can be developed with Tkinter are often quite rudimentary and primitive, in addition to exhibiting somewhat unintuitive behavior. An initial version of the developed software was created in Tkinter but was discarded when greater complexity was introduced into the software due to the difficulty of programming it. These limitations make Tkinter not the best choice for applications that require a modern and attractive user interface.

To overcome the limitations of Tkinter, QtDesigner was chosen. QtDesigner is a software that allows for the graphical design of the interface's visual part through a drag-and-drop methodology. This approach facilitates the incorporation of labels, the configuration of typography, and the definition of an appropriate color palette. One of the main advantages of QtDesigner is its ease of use, allowing users to learn how to handle it from an initial level of practically zero knowledge and progress quickly [22].

Once the visual interface is designed in QtDesigner, the files generated by this software are transformed using the PyQt5 library. PyQt5 is a Python library that enables integration with the Qt framework, used by QtDesigner. This library transforms the design files into a Python script (.py), allowing for the implementation of the application's logic. This library includes the Tkinter library by importing various functions that constitute it. Therefore, moving from using Tkinter to PyQt5 via QtDesigner was a beneficial decision because the basic knowledge acquired in that first software prototype could evolve to the final phase, reducing its complexity in terms of programming.

With PyQt5, the interconnection of the different tabs of the interface is achieved, input and output variables are managed, and the various calculations necessary for the analysis of radiation patterns are executed. This includes implementing functions to process data, update the interface in response to user actions, and present the results clearly and effectively.

6.2 Main Screen

The first step in creating the main screen for the graphical interface is to establish the layout structure of the elements. Separating the main screen into 3 frames, top bar, side bar and dashboard screen as can be seen in Figure 6.1.

Figure 6.1: Main Screen.

- The top bar is just to place the Sener icon on a background of the corporate color.
- The side bar formed by the main menu where the user can select the antenna configuration under study. This side menu to choose an option from the established configurations is formed by a pop-up drop-down button. When the user opens the screen, the menu button will appear, on

which the main array configurations will be displayed: Linear, Regular and Circular. Regular and Circular are also pop-up dropdown buttons so you can select their Regular, Shifted, Ring and Concentric subcategories respectively. This menu is made up of a pushbutton-type widget connected to the rest of the pushbuttons from a signal that allows clicking on the button to display its respective buttons and if not pressed, they remain hidden. The other option is upload a .csv file from CST even a hand-generated file. This software generates files with the positions in the three axis (X, Y and Z), the amplitude of each element and the phase. This file can be uploaded just dragging the file to the "Upload File" button located in the lower part of the side bar.

- The dashboard frame is a white space reserved for display the future results of the array configuration.

6.3 Dialog Boxes

In the previous section, the method for selecting a type of array distribution was explained. Once the topology is selected, a dialog box appears, allowing the user to input various parameters to customize the array to be analyzed, assuming it is located on the XY plane (See Figure 6.2). Within each type of array, besides the different input parameters, one can choose between two types of antennas: the rectangular patch or the circular patch, which were computationally modeled based on field equations and physical dimensions through simulation in CST, as explained in Chapter 4.

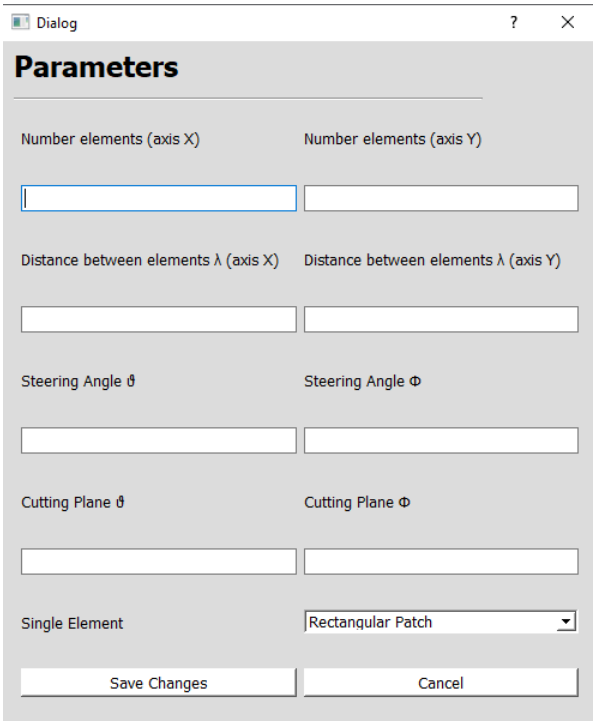

Figure 6.2: Dialog box regular parameters.

- In the linear array, parameters such as the number of elements, the distance between elements as a function of wavelength, the elevation pointing angle, and the desired plane cut can be specified. Additionally, the axis on which to place the array, either the X or Y axis, can be selected.
- In the regular planar array, parameters such as the number of elements on both axes, the distance between elements on both axes (as a function of wavelength), the elevation and azimuth pointing angles, and the field cut points where the radiation pattern will be analyzed are required.
- In the shifted planar array, the same input fields as in the regular planar array are included, with the addition of the shifting offset based on the wavelength and the axis on which the interleaving is to be performed.
- In the ring array, the required parameters include the number of elements that will form the ring, the distance of the elements from the center of the circumference based on the wavelength, the elevation and azimuth pointing angles, and the planes of cut for analyzing the radiation pattern.
- The concentric array uses the same dialog box as the ring array, with the difference that when entering the number of elements, both the elements forming the ring and the central element are considered.

All dialog boxes incorporate two buttons at the bottom of the screen: "Save Changes", which collects the data and sends it to a function to return the corresponding results, and "Cancel", which clears all information entered in the various fields on the screen. Clicking on either button closes the dialog box automatically, and to reopen it, you need to select the type of array again.

The fields to be filled in the dialog box are designed for a specific type of data; if not adhered to, the interface will fail and will not function as expected. No field can be left empty; it is mandatory to complete all parameters of the selected array type. The number of elements must be an integer greater than or equal to 2; as the number of elements increases, the time required to return a result will also increase accordingly. The distance between elements must be a decimal number greater than 0 based on the wavelength. The pointing angle in theta and phi accepts decimal numbers with a precision of up to 1 decimal, and it must be within the range [-90, 90]. The cut planes, in general, are designed for the pointing angle in elevation and azimuth; this field, due to the indexing in the graphical representation, only accepts integer values between [-90 and 90].

6.4 Main Function

The main screen interconnects with the dialog boxes that record the input data. These collect the parameters and send them to the main function. The function first determines whether the data has been collected via a .csv file to read each field from the file or if it consists of parameters collected in input variables. The next step is to calculate the electric field generated by the selected patch type,

circular or rectangular. If a file is introduced, the type of antenna used cannot be specified, so by default, the rectangular type will be assumed for subsequent calculations.

The following step is to calculate the array factor for the selected type using the expressions studied in Chapter 5, taking into account the number of elements, distances, and pointing direction. When introducing the file, the distances of the elements are extracted from the positions, the elements from the file items, and the amplitude and progressive phase are also input parameters, with the latter including the pointing direction. Amplitude is not an input parameter within the dialog boxes but is in the CST imported files; for these cases, a uniform amplitude distribution equal to 1 will be assumed.

After calculating the radiated field and the array factor, the radiation pattern is computed. Subsequently, some basic parameters of the radiation patterns are obtained, such as: maximum gain, scan losses (the losses the array has in the pointing direction relative to its maximum in the broadside direction), the SLL, and the 3dB beamwidth for the main cuts at $\phi = 0^{\text{o}}$, $\phi = 90^{\text{o}}$ and the pointing ϕ_o.

Based on the distribution, the number of elements, and the distances between them, the positions of the elements on the XY plane are dimensioned to visualize their distribution. The files contain the positions of the radiating elements themselves, making it a more immediate step to represent them on the XY plane.

This function returns to dialog box the normalized radiation pattern, the various calculations of the radiation patterns, and the positions on the XY plane. The dialog box is responsible for returning all the data received from the main function and the cut points to be analyzed to the main screen.

6.5 Dashboard Results

It was previously explained that the main screen is divided into three frames, one of which is the dashboard results frame. This frame is further subdivided into two frames: one for the graphs and another for the results of the basic calculations (see Figure 6.3). Initially, this dashboard is blank, and when results are returned, the two subdivided frames emerge. Each time a new call is made, the results are refreshed, meaning that the previous display is cleared and the new results are shown.

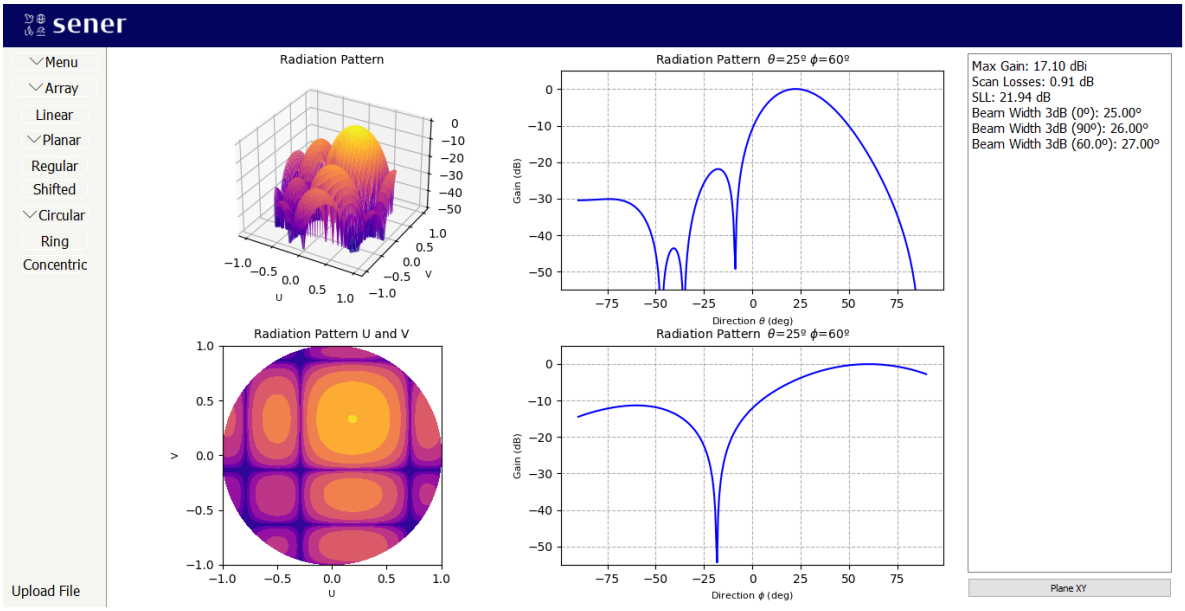

Figure 6.3: Main screen viewing results.

The graphs displayed include the radiation pattern as a function of u and v in 3D and 2D, and the radiation patterns in the cuts of the angles previously selected by the user. In the case of the linear model, being a one-dimensional array that only points in elevation, a single graph of the radiation pattern cut at the angle selected by the user is returned. The other part of the dashboard presents the results of the calculations of parameters such as maximum gain, scan losses, SLL, and the 3dB beamwidth of the main cuts, in that order. At the end of the numerical results dashboard, there is a button that, when clicked, shows an emergent tab displaying a graph of the array distribution on the XY plane (see in Figure 6.4).

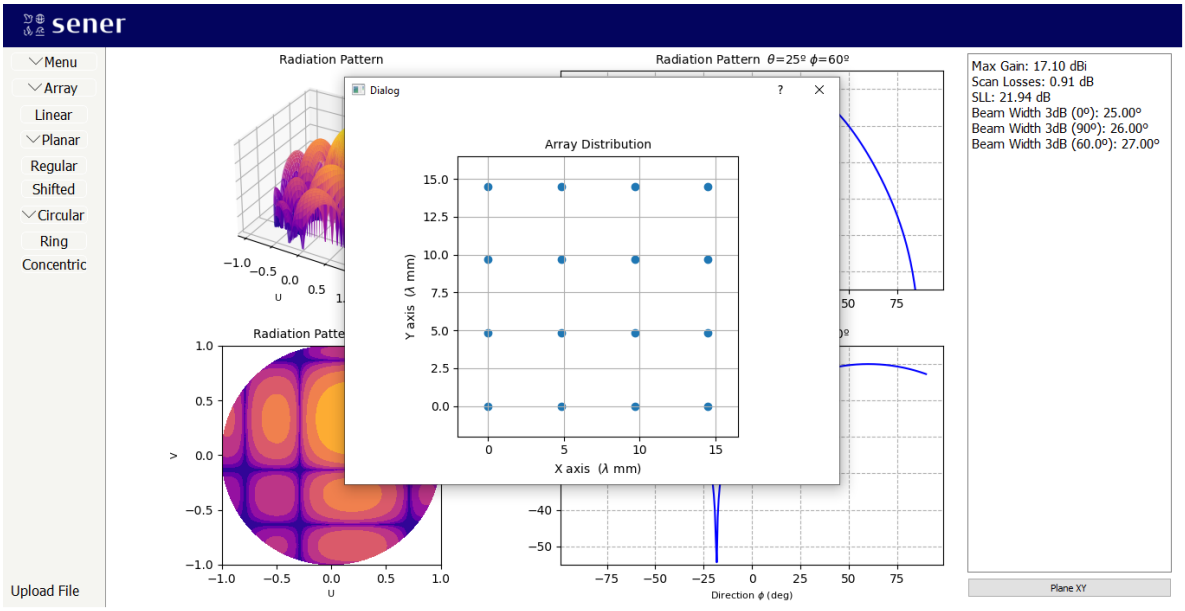

Figure 6.4: Main screen array distribution.

6.6 Example of application

In this section, an example of the application's utility is presented. For the Karfid project, it was necessary to evaluate the radiation patterns of a planar antenna configuration. Specifically, a regular arrangement of 384 x 256 antennas was used, with a separation between them of 0.58λ on both axes. Calculations were performed with the following pointing: $elevation = 10°$ and 5^{o}, $azimuth = 0°$, $45°$, and $90°$.

The number of elements on both axes, the distance between the elements on both axes, the theta and phi pointing angles, and the cutting planes were considered. A rectangular patch antenna was used as the individual element. These parameters were used to construct the requested model in the graphical interface and to evaluate the characteristics of the radiation patterns. In Figure 6.5, the evaluation of the pointing at $\theta = 10°$ and $\phi = 45°$ for this antenna array configuration is shown.

Through this example, it can be assessed that this regular arrangement of antennas, using microstrip antennas, demonstrates its scanning capability in various SAR missions. It was verified that a large array of conventional patch antennas can be evaluated for spotlight or stripmap data acquisition types, having a narrow main lobe that allows for precise targeting of a specific area to scan.

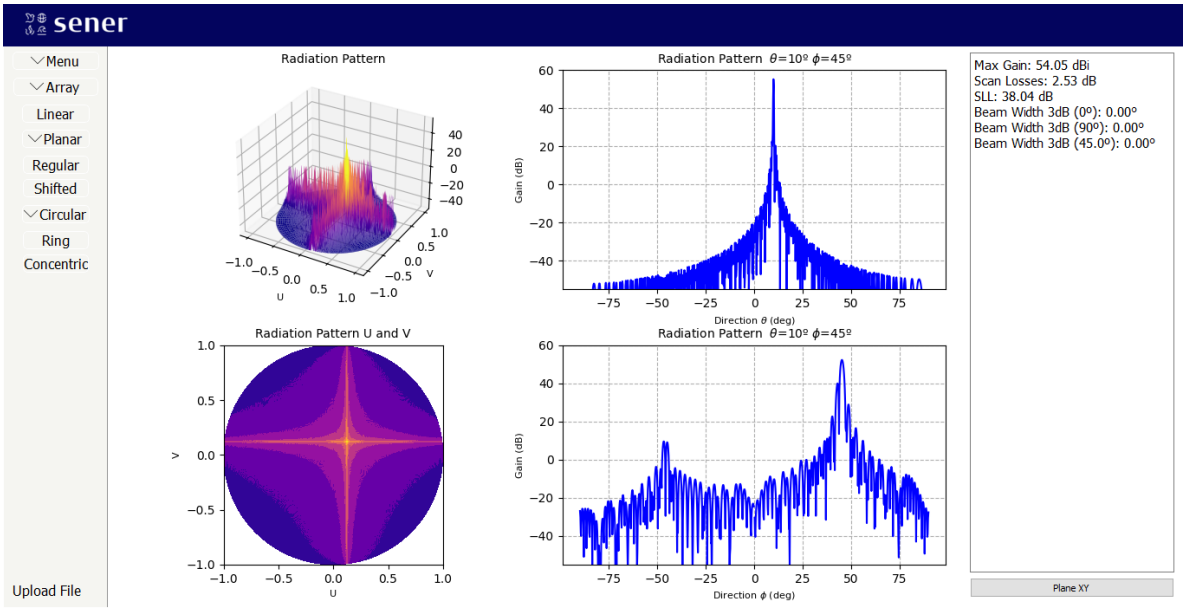

Figure 6.5: Regular planar array 256 x 384.

Chapter 7

Conclusions and Future Lines

In this project, the radiation field of canonical microstrip antennas, both rectangular and circular models, has been studied at the simulation and computational level, following the field equations established in textbooks. Subsequently, a set of antennas satisfying the needs of the Karfid project has been designed in an electromagnetic simulation environment, and then translated to the computational level based on their physical dimensions and field equations.

The behavior of the array factor has been studied for the linear model, planar with its two subgroups regular and shifted, and the circular model, also with its two subgroups concentric and ring. Fundamental properties of each model have been compared, such as maximum gain, 3dB beamwidth, SLL, or scanning losses.

The array factor of different configurations has been applied to the patches designed in the simulation environment to compare and analyze the radiation patterns of the main cuts with the array factors designed computationally. The results have been contrasted, reaching the theoretically expected results.

Finally, a graphical interface has been designed to implement configurations of the linear, planar, and circular array factor models, including their subgroups. Users can choose the type of microstrip patch and a customized arrangement of elements. The software provides radiation patterns of the designed configuration and basic parameters of that configuration as a result.

Possible future lines of expansion for this project would involve designing array factors and considering non-uniform feeding, such as tapering. This means that the feeding would be an input parameter of the software, allowing the user to feed the different elements in various ways. Additionally, positioning the elements not only in the X-Y plane but also considering other planes could be explored. Furthermore, an optimal testing and error validation phase could be developed, where incorrect values are rejected, notifying the user and resetting the data field.

Additionally, a new implementation in this application would allow, given a specific radiation pattern sought as a result, the necessary antennas and their distribution to be returned, facilitating their design for the engineer. Furthermore, the code of this application will be applied in future projects for the development of artificial intelligence based on null steering.

References

References

[1] H. Asplund, D. Astely, P. von Butovitsch, T. Chapman, M. Frenne, F. Ghasemzadeh, M. Hagström, B. Hogan, G. Jöngren, J. Karlsson, F. Kronestedt, y E. Larsson, "Chapter 4 - antenna arrays and classical beamforming," in *Advanced Antenna Systems for 5G Network Deployments*, H. Asplund, D. Astely, P. von Butovitsch, T. Chapman, M. Frenne, F. Ghasemzadeh, M. Hagström, B. Hogan, G. Jöngren, J. Karlsson, F. Kronestedt, y E. Larsson, Eds. Academic Press, 2020, pp. 89–132. [En línea]. Disponible: https://www.sciencedirect.com/science/article/pii/B9780128200469000046

[2] R. J. Mailloux, "Chapter 1 phase arrays in radar and communication systems - phase array antenna handbook," in *Phase Array Antenna Handbook*, D.Jackson, Ed. IEEE Antennas Propagation, 2018, pp. 45–56.

[3] C. A. Balains, "Antenna theory: Analysis and design, 4th edition," in *Antenna Theory: Analysis and Design*. Wiley, 2015.

[4] Cardama Aznar, *Antenas*. Barcelona: Universidad Politécnica de Cataluña, 1998, vol. 3.

[5] S. V. Hum, "RADIANCE — lab - ECE422," radio and Microwave Wireless Systems. [En línea]. Disponible: https://radiance.ece.utoronto.ca/ece422.html

[6] S. Prabir, "A quantitative analysis of the power advantage of hybrid beamforming for multibeam phased array receivers," *Analog Devices Technical Article.*, 12 2021.

[7] J. S. Herd y M. D. Conway, "The evolution to modern phased array architectures," *Proceedings of the IEEE*, vol. 104, no. 3, pp. 519–529, 2016.

[8] C. Hall, "What is Synthetic Aperture Radar?" 11 2023. [En línea]. Disponible: https://www.earthdata.nasa.gov/learn/backgrounders/what-is-sar

[9] J. Jancco-Chara, F. Palomino-Quispe, R. J. Coaquira-Castillo, J. C. Herrera-Levano, y R. Florez, "Doppler factor in the omega-k algorithm for pulsed and continuous wave synthetic aperture

radar raw data processing," *Applied Sciences*, vol. 14, no. 1, 2024. [En línea]. Disponible: https://www.mdpi.com/2076-3417/14/1/320

[10] "Satellite microwave remote sensing course," https://learninghub.esa.int/content/satellite-microwave-remote-sensing-course-may-2023, 2023.

[11] J. P. Merryman Boncori, "Measuring coseismic deformation with spaceborne synthetic aperture radar: A review," *Frontiers in Earth Science*, vol. 7, 02 2019.

[12] L. Bu, S. Zhao, G. Zhang, y R. Song, "Simulations of spotlight synthetic aperture radar super-resolution algorithm," *Journal of the Indian Society of Remote Sensing*, vol. 50, 01 2022.

[13] J. R. Rodon, "Analysis and evaluation of terrain observation by progressive scans (topsar) mode in synthetic aperture radar." pp. 49–61, 2009, trabajo final de carrera, Universidad Politécnica de Cataluña.

[14] P. Bevelacqua, "The Antenna Theory website." [En línea]. Disponible: https://www.antenna-theory.com/

[15] A. Bhattacharjee, S. Bhadra Chaudhuri, D. Poddar, y S. Chowdhury, "Equivalence of radiation properties of square and circular microstrip patch antennas," *IEEE Transactions on Antennas and Propagation*, vol. 38, no. 10, pp. 1710–1711, 1990.

[16] K. Carver y J. Mink, "Microstrip antenna technology," *IEEE Transactions on Antennas and Propagation*, vol. 29, no. 1, pp. 2–24, 1981.

[17] "CST Studio Suite - Dassault Systèmes," 2 2024. [En línea]. Disponible: https://www.3ds.com/products/simulia/cst-studio-suite

[18] "Topic 1: Printed antennas," Class notes for "Advanced topics on antenna technologies", 2023, master in Signal Theory and Communications (MSTC), Polytechnic University of Madrid.

[19] "Boundary conditions - boundaries." [En línea]. Disponible: https://space.mit.edu/RADIO/CST_online/mergedProjects/3D/special_solvopt/special_solvopt_boundary_conditions_boundaries.htm

[20] V. Zuniga, N. Haridas, A. T. Erdogan, y T. Arslan, "Effect of a central antenna element on the directivity, half-power beamwidth and side-lobe level of circular antenna arrays," in *2009 NASA/ESA Conference on Adaptive Hardware and Systems*, 2009, pp. 252–256.

[21] "tkinter — Python interface to Tcl/Tk." [En línea]. Disponible: https://docs.python.org/es/3/library/tkinter.html

[22] "Quick start - Qt for Python." [En línea]. Disponible: https://doc.qt.io/qtforpython-6/quickstart.html